A new X-ray diffractometer for the online monitoring of epitaxial processes

Der Fakultät für Naturwissenschaften
der Universität Paderborn
zur Erlangung des akademischen Grades eines
Doktors der Naturwissenschaften (Dr. rer. nat.)
vorgelegte

Dissertation

von

Alexander Kharchenko

Paderborn, July 2003

Abstract

In this thesis I present an *in situ* X-ray diffractometer for X-ray diffraction analysis of epitaxial layers during metal-organic chemical vapor deposition. The conception of the *in situ* X-ray diffractometer, the model of data interpretation and the description of the experimental setup are given in detail. The diffractometer has been constructed and tested under laboratory conditions with wurtzite type AlGaN- and InGaN-based materials. The results of tests show that the diffractometer allows to perform X-ray diffraction measurements under conditions present in a metal-organic chemical vapor deposition reactor and to obtain accurate information about the composition and relative thickness (growth rate) of epitaxial layers. The results of measurements have been compared with the results obtained by conventional high resolution X-ray diffractometer and perfect agreement has been reached.

The diffractometer has been developed without a goniometer stage. It is not sensitive to precise alignment of the samples before measurements and it has very short data collection time (up to factor 100 less than by standard diffractometers). These additional features of the X-ray diffractometer makes it well suited for extremely fast post-growth diagnostics of multilayer semiconductor structures. This potential of the diffractometer has been tested with different materials systems which are important in the semiconductor industry today, namely wurtzite AlGaN single heterostructures, wurtzite InGaN-based multiple quantum wells and SiGe heterostructures. The measurements of the line scans as well as of reciprocal space maps are presented and analyzed in terms of composition, periodicity of the multilayers and status of strain. All results are in good agreement with the results obtained by conventional high resolution X-ray diffraction.

Contents

List of Figures

List of Tables

1 Introduction

The importance of semiconductor structures for the fabrication of devices in electronics and optoelectronics is obvious. Today, billions of transistors, LEDs and sensors are manufactured weekly. Generally, the growth of semiconductor multilayer structures are realized by metal-organic chemical vapor deposition (MOCVD) or molecular-beam epitaxy (MBE). The technological process of growth demands methods for characterization and quality control. X-ray diffraction remains one of the important methods of characterization because it is non-destructive, informative and has clear interpretation. Since the discovery of X-rays in 1895 by Wilhelm Conrad Roentgen and the discovery of X-ray diffraction by Max von Laue in 1912, X-ray diffraction has been developed into a powerful tool for investigation of semiconductor materials. Nowadays, novel X-ray diffractometers equipped with high power sources and high efficiency monochromators, detectors and analysers are being produced in a large amount. They provide access to important parameters of semiconductors such as composition, strain, thickness and structural quality. There exist a huge amount of experimental and theoretical papers about the X-ray analysis of different kinds of semiconductor materials, however, most of them are dealing with post-growth characterization (see for instance reviews on high resolution X-ray diffraction [1], [2]), i.e. X-ray measurements are performed after the growth of the samples. Yet *in situ* characterization techniques are highly demanded especially for the MOCVD technology, because high ambient pressure preclude the use of electron diffraction, which is already well established for online monitoring of the MBE growth. Furthermore, X-ray diffraction is attractive as *in situ* technique because of the simple procedure of data interpretation. From the angular positions and shapes of diffraction peaks the structural information becomes easily available.

Only a few experimental X-ray investigations of semiconductors during the growth process have been reported ([3], [4], [5], [6], [7], [8], [9], [10], [11]). However, they all were carried out with synchrotron radiation where a specially designed growth chamber was brought to synchrotron sources. It is obvious that such studies are not applicable to most commercial and scientific MOCVD reactors. The intention of this work was to construct an *in situ* X-ray diffractometer (IXRD) which is suited for X-ray diffraction analysis of semiconductor layers during MOCVD growth. The apparatus has been built and tested under laboratory conditions. The results of the tests show that our *in situ* X-ray diffractometer fulfills all requirements which are important for an analysis of epitaxial layers during MOCVD growth: (1) no synchrotron radiation is needed for X-ray measurements; (2) no parts of the diffractometer are necessary inside the growth reactor; (3) the setup is able to collect X-ray patterns from rotating and wobbling samples; (4) the data collection time from rotating samples is in the order of one minute and corresponds to the deposition time of a 10 nm thick layer. Furthermore, the short data collection time (about 100 times less than with commercially available diffractometers) and the ability to measure X-ray diffraction without precise adjustment of the sample makes the equipment also well suited for extremely fast post-growth characterization of multilayer structures.

The thesis is organized as follows. Chapter 2 describes some important aspects of high resolution X-ray diffraction. The conception of a new IXRD is introduced in chapter 3. Chapter 4 describes the details of the experimental setup. Then I will proceed with chapter 5 where I show the results of tests of the IXRD for fast post-growth characterization as well as the results of measurements under conditions similar to those in a MOCVD reactor. Finally, the main conclusions are given in chapter 6.

2 Some important aspects of high resolution X-ray diffraction

2.1 High resolution X-ray diffraction in real and reciprocal space

Bragg formulated [12] the condition of diffraction of X-rays by a periodic arrangement of atoms in a solid state crystal:

$$2 \cdot d_{hkl} \cdot \sin(\Theta_B) = n \cdot \lambda \tag{2.1}$$

where d_{hkl} is the spacing between lattice planes with Miller indices (hkl), Θ_B is the Bragg angle and λ is the wavelength of X-rays.

It is a convenient and common way to describe X-ray diffraction in reciprocal space. The reciprocal lattice is formed by the terminal points of reciprocal repetition vectors $\vec{b_1}$, $\vec{b_2}$ and $\vec{b_3}$ which are related to the primitive vectors of crystal lattice $\vec{a_1}$, $\vec{a_2}$ and $\vec{a_3}$ by:

$$\vec{b_i} = 2 \cdot \pi \cdot \frac{\vec{a_j} \times \vec{a_k}}{\vec{a_1} \cdot (\vec{a_2} \times \vec{a_3})}, \quad i, \quad j, \quad k \quad cycl. \tag{2.2}$$

In reciprocal space the plane with Miller indices (hkl) is described by the reciprocal vector which is given by:

$$\vec{G_{hkl}} = h \cdot \vec{b_1} + k \cdot \vec{b_2} + l \cdot \vec{b_3} \tag{2.3}$$

The condition of diffraction 2.1 by the plane (hkl) can be reformulated in reciprocal space (see for example [13]) in the form:

$$\vec{Q} = \vec{G_{hkl}} \tag{2.4}$$

$\vec{Q}$ is the scattering vector defined as $\vec{Q} = \vec{k_\varepsilon} - \vec{k_\delta}$ where $\vec{k_\delta}$ and $\vec{k_\varepsilon}$ are the wave vectors of incident and diffracted waves as indicated in figure 2.1.

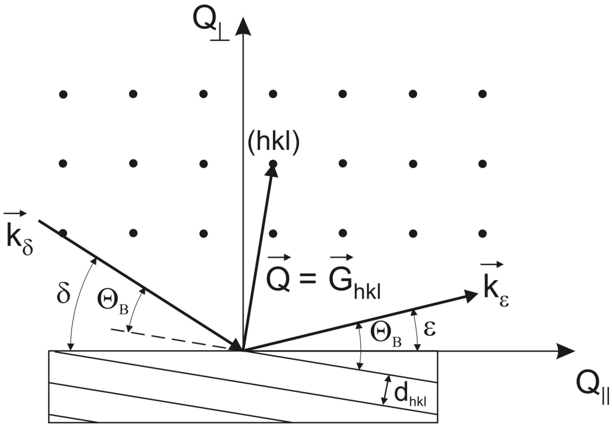

Figure 2.1: Sketch of the diffraction geometry. The exact Bragg condition for (hkl) planes is fulfilled, if the end of scattering vector $\vec{Q}$ ends at a reciprocal lattice point (hkl).

Thus in reciprocal space the diffraction plane is represented as a reciprocal lattice point and the diffraction geometry defined by the incident and by the detection angles is represented by the scattering vector. When the scattering vector ends at a reciprocal lattice point (hkl) the exact Bragg condition is satisfied. Scattered X-ray intensity around a reciprocal lattice point (RLP) is strongly influenced by the structural properties of crystalline material. Therefore, the measurement and detailed analysis of diffracted intensity around reciprocal lattice points is the subject of high resolution diffractometry. The variation of incident and detection angles allows to scan scattered intensity around the reciprocal lattice point. Depending on the required information the analysis of one or two dimensional projections of the intensity distribution around reciprocal lattice points is performed. Usually these are $\omega - 2\Theta$, ω scans [1] or two dimensional intensity distributions of reciprocal lattice points which are called reciprocal space maps.

2.2 Theory of X-ray diffraction

Generally there are two possible ways for the theoretical description of X-ray diffraction in crystals which depend on the methods for representing a crystalline structure. In the first method, the calculation of X-ray diffraction is performed by the summation of the scattered intensity from separate atoms (see for example [13], [14]). In this case the scattered intensity is proportional to the square of the structure factor given by:

$$F = \sum f_j \cdot exp(i\vec{Q}\vec{R}_j) \tag{2.5}$$

where f_j are the atomic scattering factors and summation is performed over all atoms in the unit cell. The theory of X-ray diffraction in such a form usually completely neglects the dynamical effects of X-ray diffraction which is the multiple scattering effect (extinction). For this reason it is called kinematical theory and it is not valid for a highly perfect type of crystals. The dynamical effects have been taken into account only in the theory of Darwin developed in 1914 [15].

In the second alternative formalism which has been proposed by Ewald [16] and Laue [17] the X-ray diffraction theory involves the solution of the Maxwell equations in a medium with a periodic dielectric function. In this case the electromagnetic field is represented by the Bloch functions and the dielectric constant is expressed by a Fourier series. A general description of this theory can be found in [18]. The alternative description was developed by Takagi [19], [20] and Taupin [21] where the solution is represented by Bloch functions with constant phases and with slowly varying amplitudes. Both formalisms are widely used for the calculation of X-ray diffraction spectra. In this work, I have used the Takagi-Taupin formalism for the simulation of X-ray patterns in multilayer structures which is described in [22].

2.3 Use of reciprocal space mapping for evaluation of strain status

The growth of an epitaxial film on a thick substrate causes the modification of the lattice parameter of the epilayer in growth direction due to the strain. Let a_S and c_S be the lattice parameters of a substrate crystal in direction perpendicular and parallel to the sample surface. a_0, c_0 and a, c are in-plane and perpendicular lattice parameters of bulk and grown layer respectively. Depending on the lattice mismatch between substrate and layer crystals, one distinguishes between compressive ($a_0 > a_S$) and tensile strains ($a_0 < a_S$). The lattice parameter c is increased for compressive strain and decreased for tensile strain. If the layer thickness is below a so-called critical thickness the growth is pseudomorphic and the layer is fully strained on the substrate. With increasing layer thickness the elastic energy increases. If the layer thickness is above its critical value, misfit dislocations are formed and the layer starts to relax.

Reciprocal space mapping offers the unique possibility to perform detailed investigation of the relaxation process. In figure 2.2 a) a two dimensional projection of reciprocal space in the $(Q_{||}, Q_{\perp})$ plane is shown where $Q_{||}$ and $Q_{\perp}$ are components of the reciprocal vector which are parallel and perpendicular to the sample surface.

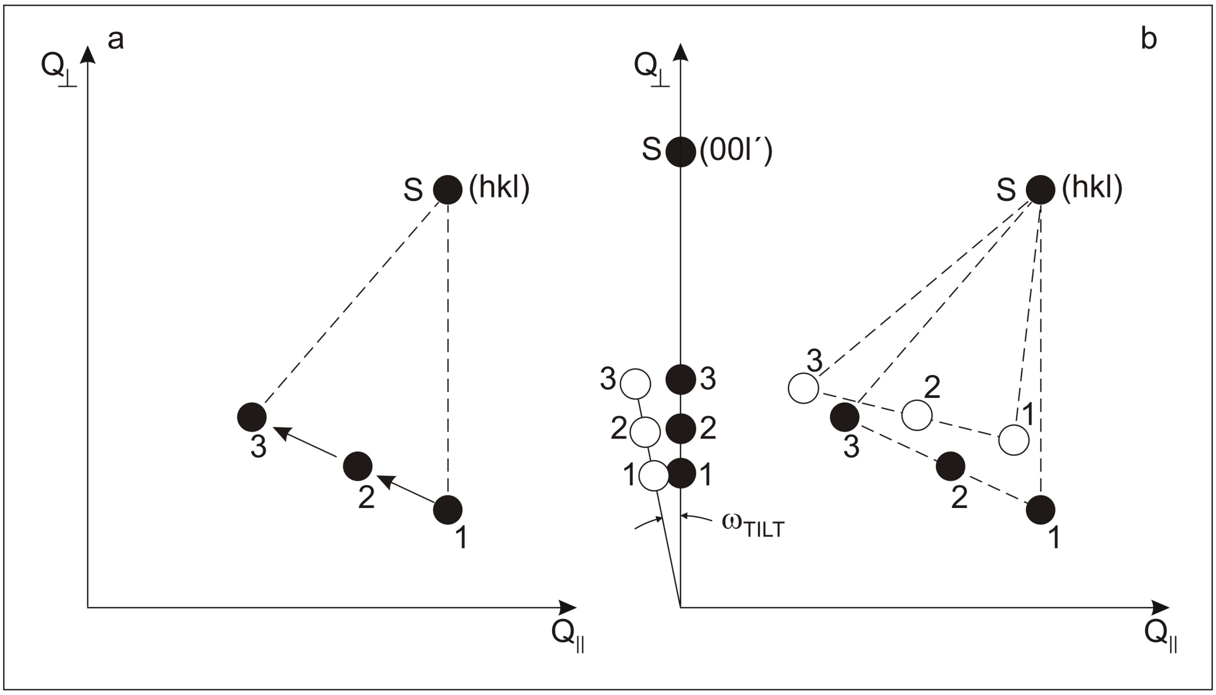

Figure 2.2: a) the effect of strain on the asymmetrical reciprocal space maps is illustrated. The positions 1, 2, 3 of the reciprocal lattice point correspond to the strained, partially relaxed and relaxed layer. b) a tilt of the layer causes a shift of reciprocal lattice points and can lead to a wrong data interpretation. The information on the layer tilt can be obtained from a symmetrical reciprocal space map.

We consider (hkl) reflection for which $l \neq 0$ and h or $k \neq 0$, because for this case the position of reciprocal lattice point depends on both in-plane and perpendicular lattice parameters. Point S is the reciprocal lattice point of the substrate crystal. The points 1, 2 and 3 correspond to the reciprocal lattice point of layer which has different states of strain. Below the critical thickness the layer is fully strained. This means that in-plane lattice parameters of layer and substrate are identical ($a = a_S$) and the vertical lattice parameter of the layer increases ($c > c_0$). In reciprocal space this corresponds to position 1 of the RLP of the layer. Due to the relaxation the strain is relieved therefore the in-plane constant of layer increases and the perpendicular constant decreases (position 2) until finally the bulk lattice parameters are reached (position 3). The position of the reciprocal lattice point of the layer depends on the lattice parameter and therefore reciprocal space mapping is an ideal method for strain analysis. However, the measurement of only one asymmetrical reflection can lead to a wrong interpretation due to a possible crystallographic tilt of the lattice planes. In figure 2.2 b we demonstrate the situation in reciprocal space where the positions of layer reflections are shown with and without tilt. It is not possible to distinguish between effect of strain and tilt of the layer. One possibility to identify the crystallographic tilt of the layer is to measure a symmetrical reflection (00l). As shown in figure 2.2 b, in case of a symmetrical reciprocal space map a tilt of the layer causes the deviation of RLPs from the vertical axis $Q_\perp$. The tilt angle ω_{TILT} which can be determined from the symmetrical reflection allows to separate the effect of strain and tilt of the layer. Thus, measuring both asymmetrical (hkl) and symmetrical (00l) reflections the effect of strain and crystallographic tilt can be investigated in detail.

2.4 Use of reciprocal space mapping for determination of chemical composition of ternary compounds

Let us assume that a ternary epilayer $A_xB_{1-x}C$ is deposited on a substrate S. The epilayer is an alloy of the binary compounds AC and BC. We consider the general situation when alloy $A_xB_{1-x}C$ has arbitrary status of strain so that $A_xB_{1-x}C$ can be relaxed, partially relaxed or strained. Compound AC and BC have in-plane and perpendicular lattice parameters a_{AC}, c_{AC} and a_{BC}, c_{BC}, respectively. Our considerations will be valid for two type of structures which are of importance in this work: zincblende structures with tetragonal symmetry and wurtzite type structures with hexagonal symmetry. For the cubic symmetry the in-plane and perpendicular lattice parameters should be assumed identical. By measuring the symmetrical and asymmetrical reciprocal space maps we get reliable information about in-plane and perpendicular lattice parameters of epilayer a and c taking into account the effect of a possible crystallographic tilt as described in the previous section. a_0, c_0 are lattice parameters of the relaxed $A_xB_{1-x}C$ alloy, i.e., lattice parameters of unstrained layer. We assume that there is a linear relationship between lattice parameters of the relaxed alloy $A_xB_{1-x}C$ and the lattice parameters of AC, BC compounds and the composition x (Vegard's law):

$$\begin{aligned} a_0 &= x \cdot a_{AC} + (1-x) \cdot a_{BC} \\ c_0 &= x \cdot c_{AC} + (1-x) \cdot c_{BC} \end{aligned} \tag{2.6}$$

In order to find the relationship between relaxed lattice parameters a_0, c_0 of $A_xB_{1-x}C$ alloy and measured lattice parameters a and c the effect of strain has to be considered. It can be described using the elasticity theory [23], [24]. The deformation state of a crystal is described by the strain tensor ε_{ij} which is related to the stress tensor σ_{ij} by the tensor of stiffness constants. In the case of biaxial strain, the stress normal to the film vanishes and the following relation between strain in the growth direction and the in-plane strain is obtained:

$$\frac{c-c_0}{c_0} = -\nu(x) \cdot \frac{a-a_0}{a_0} \tag{2.7}$$

where $\nu(x)$ is Poisson's ratio which is:

$$\begin{aligned} \nu(x) &= 2 \cdot \frac{C_{12}(x)}{C_{11}(x)} \quad for \quad tetragonal \quad symmetry, \\ \nu(x) &= 2 \cdot \frac{C_{13}(x)}{C_{33}(x)} \quad for \quad hexagonal \quad symmetry. \end{aligned}$$

C_{ij} are the elements of the tensor of the elastic moduli (stiffness constants) in Voigt's notation which depend on the composition x. The general assumption is a linear dependence of stiffness constants on the composition x. The chemical composition x is obtained by substitution of expressions 2.6 for a_0 and c_0 in 2.7. In case of a linear dependence of stiffness constants on the composition x, this leads to an equation of degree four for x. The solution is possible only by numerical methods.

In the first-order approximation used in [25] a linear relation for Poisson's ratio is applied:

$$\nu(x) = x \cdot \nu_{AC} + (1-x) \cdot \nu_{BC} \tag{2.8}$$

In this case a cubic equation for x is obtained. As shown in [25], in this case the analytical solution is straightforward following the formula of Abramowitz and Stegun. There are three real solutions, but only one physically meaningful value of x exists.

If the elastic constants of two compounds AC and BC do not differ too much or if x is close to zero or unity it is a good approximation to assume that the elastic moduli do not vary with the chemical composition. Then substitution of 2.6 for a_0 and c_0 in 2.7 results in a quadratic equation:

$$Px^2 + Qx + R = 0 \tag{2.9}$$

where

$$\begin{aligned} P &= \nu \cdot \Delta a \cdot \Delta c + \Delta a \cdot \Delta c, \\ Q &= \nu \cdot \Delta a \cdot c_{BC} - \nu \cdot \delta a \cdot \Delta c + \Delta c \cdot a_{BC} - \Delta a \cdot \delta c, \\ R &= -\nu \cdot \delta a \cdot c_{BC} - \delta c \cdot a_{BC}, \end{aligned}$$

and $\Delta a = a_{AC} - a_{BC}, \quad \Delta c = c_{AC} - c_{BC}, \quad \delta a = a - a_{BC}, \quad \delta c = c - c_{BC}$.

The solution for x is unique and is given by:

$$x = \frac{-Q - \sqrt{Q^2 - 4 \cdot P \cdot R}}{2 \cdot P} \tag{2.10}$$

In this thesis we have measured semiconductor structures with ternary layers with a mole fraction x of less than 0.25. Therefore approximation 2.9 has been used for the calculation of the chemical composition. The lattice parameters and stiffness constants for the relevant materials are given in appendix A.

3 Conception of an in situ X-ray diffractometer for online monitoring of the MOCVD growth process

3.1 Requirements for IXRD and basic principles of an IXRD

As I have mentioned in the introduction, X-ray diffraction is a very promising tool for online controlling of the MOCVD growth process. However, the application of X-ray diffraction for *in situ* monitoring of the MOCVD growth process is a challenging task. The measurement conditions are complicated due to the construction of the growth reactor and the conditions of growth so that they are not ordinary for standard X-ray diffractometers. There are two ways for the solution of this problem. Previously, specially designed growth chambers have been developed and brought to the synchrotron laboratories ([3]-[11]). The drawback of such a solution is obvious, *in situ* X-ray diffractometers can not be widely used for commercial as well as for scientific purposes.

The second solution is the development of a specially designed X-ray diffractometer which can be installed on a MOCVD reactor. Knowing the construction of a MOCVD reactor and the conditions of growth we formulate below the requirements for such an *in situ* X-ray diffractometer:

- no parts of the diffractometer for adjustment and positioning of the samples should be necessary inside the growth chamber. That allows to avoid any complications to the construction of the MOCVD reactor and any disturbances of the growth process. For the X-ray diffraction setup this means that IXRD should not be sensitive to the precise alignment of the samples and should not require the positioning of the samples during measurements;

- the IXRD has to be able to collect spectra from rotating and wobbling samples. This requirement is especially important, because samples are rotated during MOCVD and wobbling of the samples can not be excluded during the growth process;

- the setup should provide a data collection time which is at least comparable to the typical deposition time of several nanometer thick layers in a MOCVD reactor.

The design of an IXRD setup is the goal of this thesis. The key features of our IXRD are: i) the use of focused monochromatic X-ray beams impinging onto the sample instead of a goniometer system and ii) to collect the diffracted X-rays by a multichannel detector.

To get focused monochromatic beams we use a Johansson monochromator. The principles of the Johansson monochromator are described in the original paper of T. Johansson [26]. The diffracting planes of a crystal are bent with a radius 2R and the surface of the crystal forms a cylinder with a radius R as indicated in figure 3.1.

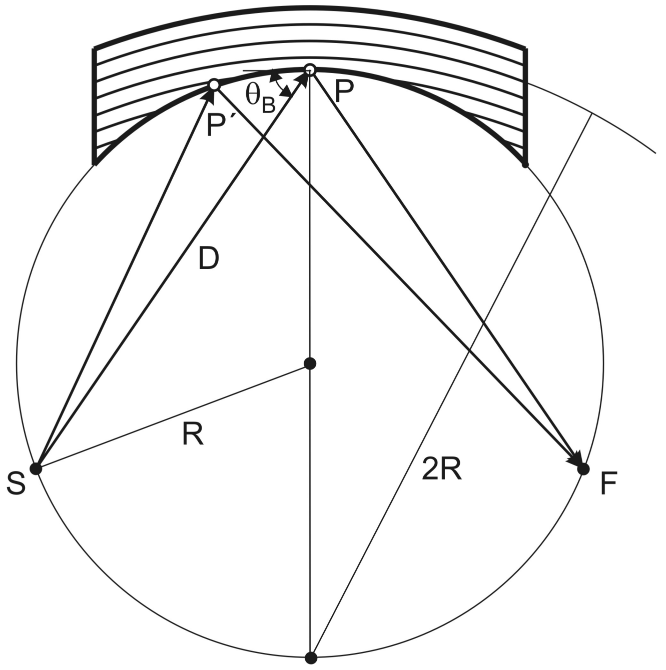

Figure 3.1: The principle of the Johansson monochromator. The beams coming from a X-ray source S are monochromized and focused at the point F by the Johansson monochromator.

When the X-ray source is located at point S on the circle R which is usually called Rowland circle, all beams strike the lattice planes of the crystal at the same angle. All reflected beams are focused at point F lying on the Rowland circle. Thus the Johansson monochromator allows to get monochromatic and focused X-ray beams provided two conditions are fulfilled. Firstly, X-ray source, monochromator crystal and sample are placed on the Rowland circle. Secondly, the angle of incidence equals the Bragg angle of the monochromator crystal. The second condition gives the relation between the radius of the Rowland circle, Bragg angle and the distance between X-ray source and the center of the monochromator:

$$D = 2 \cdot sin(\Theta_B) \cdot R \tag{3.1}$$

The sample to be investigated with the IXRD setup is placed at the focusing point F. After diffraction the scattered X-rays are collected by a multichannel detector.

3.2 IXRD in terms of reciprocal space

The scattering geometry of IXRD in real space is schematically illustrated in figure 3.2 a. Here we have to distinguish between two important angles: incident angle δ and detection angle ε. Incident angle δ is the angle between incident beam and the sample surface. Detection angle ε corresponds to the angle between direction of the detection of scattered intensity and the sample surface. The formation of the measurement point in IXRD is indicated in figure 3.2 (a): the bunch of monochromatic X-rays with incident angles between δ and $\delta + \Omega$ strikes the sample. The scattered beams are measured by one certain channel of a multichannel detector under a detection angle ε.

Figure 3.2 (b) shows the geometry of IXRD in reciprocal space. The beam with the incident angle δ and the beam with the detection angle ε are described in reciprocal space by the wave vectors $\vec{k_\delta}$ and $\vec{k_\varepsilon}$, respectively. Because the incident beams are monochromatic and we are interested in an elastic scattering, the lengths of wave vectors $\vec{k_\delta}$ and $\vec{k_\varepsilon}$ are the same. In reciprocal space the scattered intensity is plotted as a function of the scattering vector which is defined as $\vec{Q} = \vec{k_\varepsilon} - \vec{k_\delta}$. In our setup one measurement point is accomplished by the wave vector $\vec{k_\varepsilon}$ and the endpoints of the incident wave vectors between $\vec{k_\delta}$ and $\vec{k_{\delta+\Omega}}$ as indicated in figure 3.2 b. The corresponding scattering vectors $\vec{Q}$ describe in reciprocal space a line depicted in figure 3.2 b as "detection window". The construction in reciprocal space shows that the intensity measured by one channel of the detector array is the sum of scattered intensity distributed in reciprocal space within the "detection window".

In figure 3.3 (a) we consider two different measurement points 1 and 2. The scattered

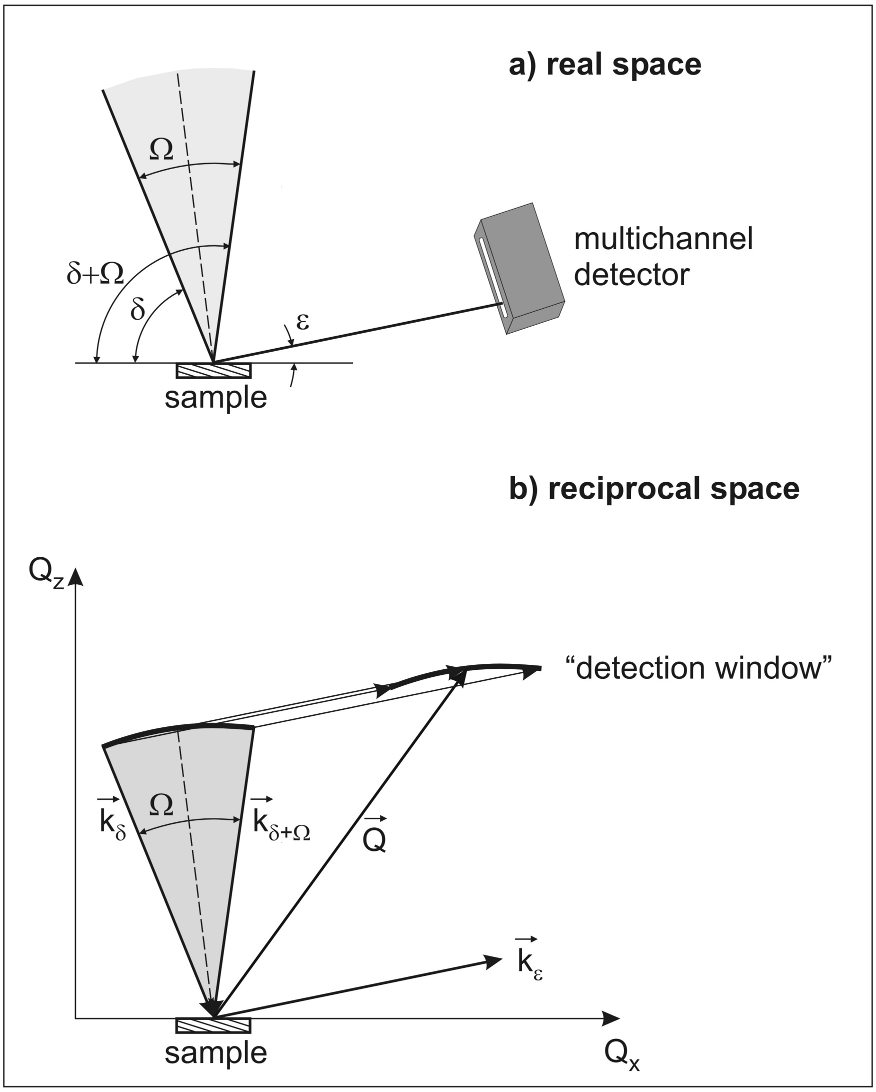

Figure 3.2: The geometry of the IXRD setup in real (a) and reciprocal (b) space. One measurement point in the IXRD setup is described in angular space by the certain detection angle ε and by the bunch of incident waves with angular aperture Ω. In reciprocal space this configuration corresponds to the line called "detection window".

intensity at two different channels which correspond to the detection angles ε_1 and ε_2. Figure 3.3 b demonstrates the situation in reciprocal space: the corresponding scattering vectors $\vec{Q}_1$ and $\vec{Q}_2$ describe lines "detection window 1" and "detection window 2", respectively. In this case, the intensities of measurement points 1 and 2 in IXRD setup are the intensities distributed within "detection window 1" and "detection window 2", respectively. The centers of the "detection windows" are located on the line shown in

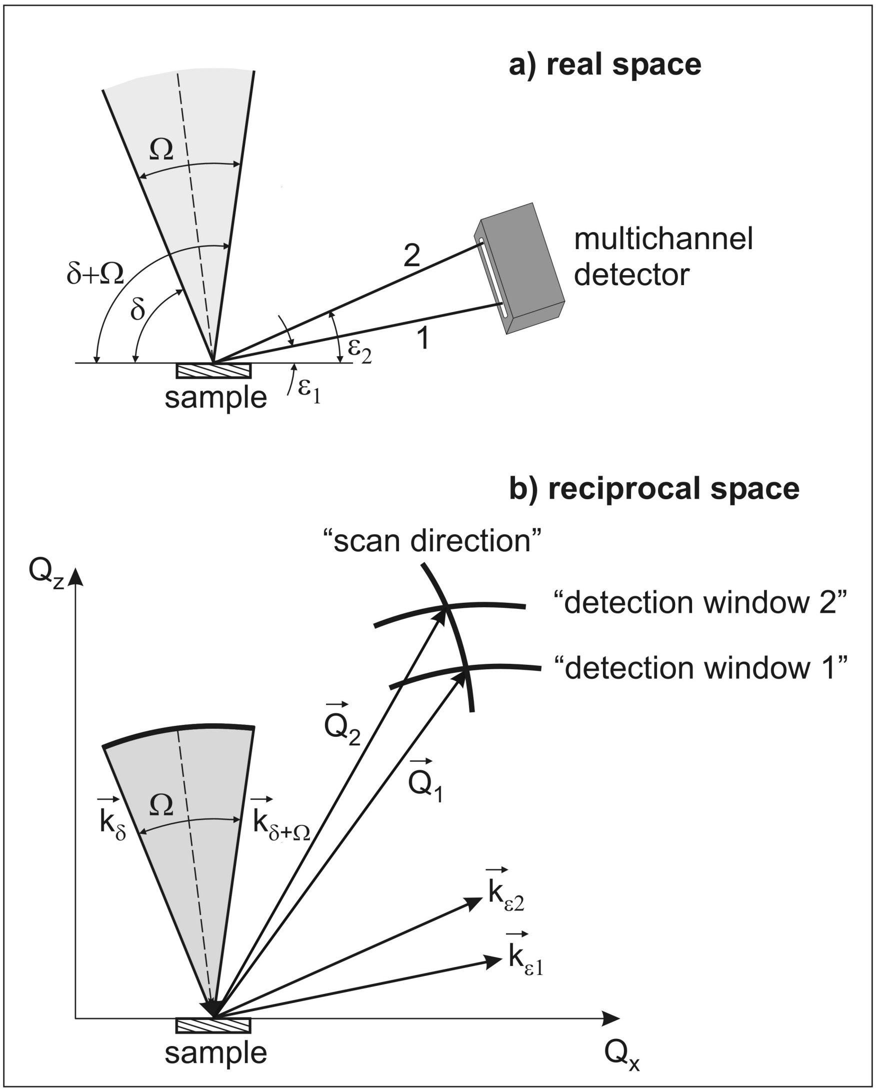

Figure 3.3: The geometry of the IXRD setup in real (a) and reciprocal (b) space for two measurement points. The different measurement points are described in angular space by the two different detection angles ε_1 and ε_2. In reciprocal space each measurement point can be associated with the line "detection window". The direction of measurement in the IXRD setup is described by the line "scan direction".

figure 3.3 b as "scan direction". This means that the change in the detection angle ε results in a shift of the scattering vectors along the "scan direction".

In figure 3.4 a, b we show the measurement results of an AlGaN/GaN heterostructure performed with the IXRD setup and the intensity distribution in reciprocal space measured by a conventional high resolution equipment. The X-ray intensity measured with the IXRD setup is plotted as a function of the relative detection angle $\Delta\varepsilon$. The zero value of the $\Delta\varepsilon$ angle is set to the position of the GaN peak. Each measurement point in the IXRD setup can be associated with the "detection window" in reciprocal space as shown for two arbitrary points 1 and 2 in figure 3.4. The angular distance $\Delta\varepsilon$ between two points 1 and 2 in the IXRD spectrum is related to the distance ΔQ_{IXRD} along the "scan direction" in reciprocal space.

The reciprocal space coordinates are related to the incident angle δ and the detection angle ε by the following expressions:

$$\begin{aligned} Q_x &= \frac{2\cdot\pi}{\lambda}\cdot(\cos(\varepsilon)-\cos(\delta)) \\ Q_z &= \frac{2\cdot\pi}{\lambda}\cdot(\sin(\varepsilon)+\sin(\delta)) \end{aligned} \tag{3.2}$$

Distance ΔQ_{IXRD} along the "scan direction" is formed by keeping fixed the incident angle $\delta = \delta_o$ and varying the detection angle from ε_{br} to $\varepsilon_{br}+\Delta\varepsilon$ where ε_{br} is the detection angle corresponding to the Bragg reflection of GaN. Therefore ΔQ_{IXRD} corresponds to the change of coordinates Q_x and Q_z by the values ΔQ_x and ΔQ_z which are given by:

$$\begin{aligned} \Delta Q_x &= \frac{2\cdot\pi}{\lambda}\cdot(\cos(\varepsilon_{br}+\Delta\varepsilon)-\cos(\varepsilon_{br})) \\ \Delta Q_z &= \frac{2\cdot\pi}{\lambda}\cdot(\sin(\varepsilon_{br}+\Delta\varepsilon)-\sin(\varepsilon_{br})) \end{aligned}$$

If the relative detection angle $\Delta\varepsilon$ is small we can use:

$$\begin{aligned} \Delta Q_x &= -\frac{2\cdot\pi}{\lambda}\cdot\sin(\varepsilon_{br})\cdot\Delta\varepsilon \\ \Delta Q_z &= \frac{2\cdot\pi}{\lambda}\cdot\cos(\varepsilon_{br})\cdot\Delta\varepsilon \end{aligned}$$

The length ΔQ_{IXRD} is thus:

$$\Delta Q_{IXRD} = \sqrt{\Delta Q_x^2 + \Delta Q_z^2} = \frac{2\cdot\pi}{\lambda}\cdot\Delta\varepsilon \tag{3.3}$$

The expression 3.3 connects the angle between measurement points in the IXRD spectrum and the corresponding distance ΔQ_{IXRD} in reciprocal space along the "scan direction". It should be emphasized that the orientation of "scan direction" and "detection window" in reciprocal space strongly depends on the diffraction geometry of the IXRD setup. Therefore the information which can be obtained by the IXRD setup is different for different scattering geometry. To find out the diffraction geometry which is suitable for the determination of vertical and lateral lattice parameters, a model for the interpretation of measurements with the IXRD setup will be developed in the next section.

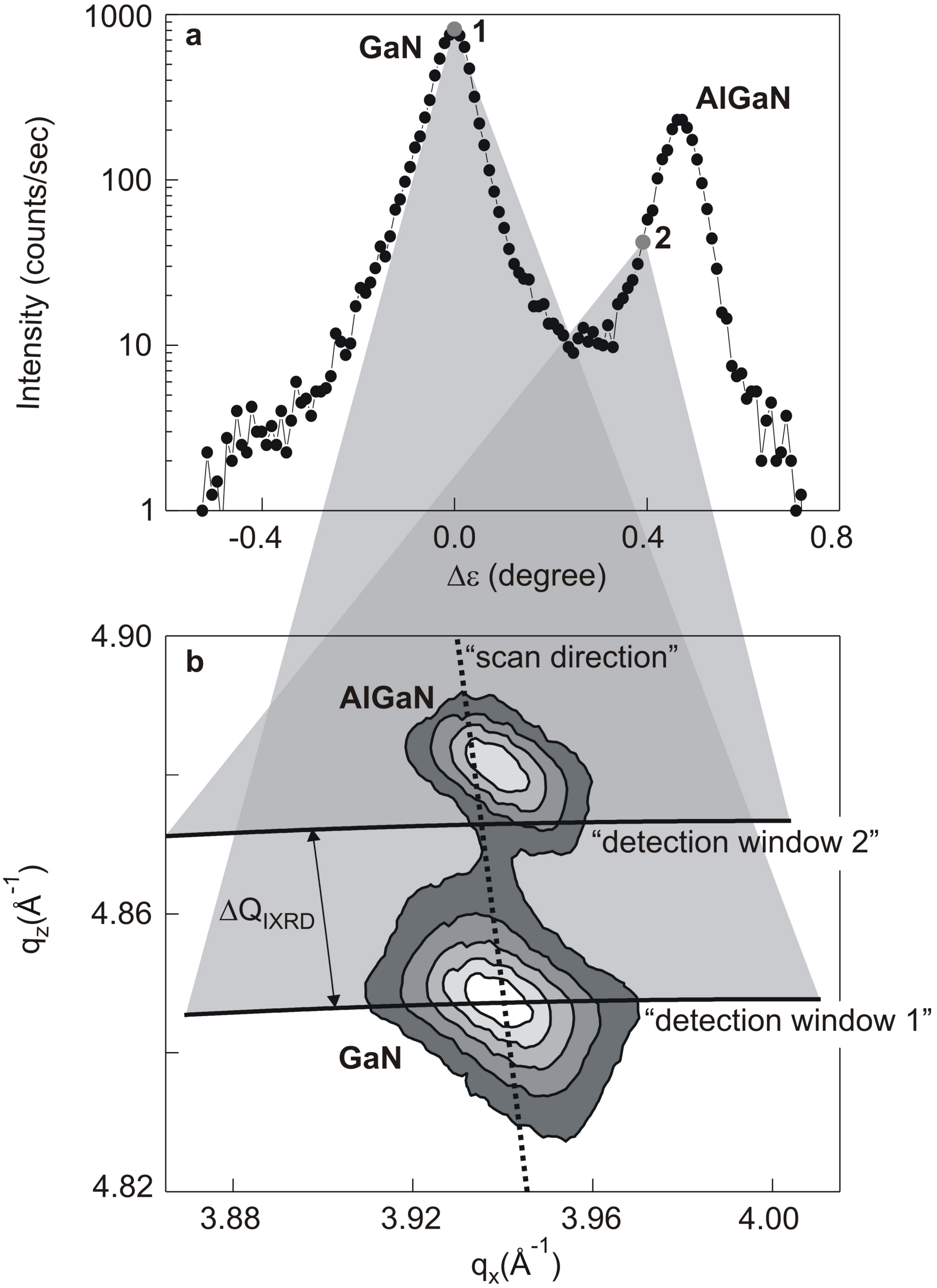

Figure 3.4: Illustration of measurement principles of the IXRD setup. a) intensity measured by the IXRD setup plotted as a function of the relative detection angle $\Delta\varepsilon$, b) the intensity distribution in reciprocal space measured by a standard high resolution equipment. The relative detection angle $\Delta\varepsilon$ is related to the distance ΔQ_{IXRD} in reciprocal space along the "scan direction".

3.3 Interpretation of measurements with IXRD

3.3.1 Choice of suitable diffraction geometry

Our aim is to investigate a certain multilayer crystal structure with the IXRD setup. Let us consider the general situation in reciprocal space shown in figure 3.5. We assume that there is a crystal present in a multilayer structure which lattice parameters are known. This means that we know the position of the reciprocal lattice point of this crystal in reciprocal space. We will denote this crystal as a "substrate crystal" and will use it as a reference point in reciprocal space. The point "S" is the center of distribution of the intensity diffracted from this crystal.

For simplicity reasons we restrict ourselves to the consideration of only one reflection "M" which is the result of scattering from a multilayer structure. It can be, for example, a reflection from a crystalline layer included in a multilayer structure or a satellite peak of a superlattice structure, etc. As full lines we depict the "detection windows" corresponding to different measurement points of the detector and the bold dashed line denotes the "scan direction".

As described in the previous section the IXRD setup provides information about the distance ΔQ_{IXRD}. However, the distances between reflections along the Q_z and Q_x axes (hereafter vertical ΔQ_z and lateral ΔQ_x distances, respectively) are required because they provide access to the lateral and vertical lattice parameters of crystalline layers. In case of a single layer, for example, they directly provide the lattice parameters parallel and perpendicular to the sample surface. In case of a superlattice structure they yield the average lattice parameter of barrier and well layers. Furthermore, in case of a periodical structure the distances between reflections in Q_z and Q_x directions can additionally provide information about the periodicity of the structure.

Thus our aim is to find the vertical distance ΔQ_z and the lateral distance ΔQ_x using the distance ΔQ_{IXRD} which is measured with the IXRD setup. From geometrical considerations we get the following relations between the vertical distance ΔQ_z, the lateral distance ΔQ_x, and the distance ΔQ_{IXRD}:

$$\Delta Q_z = \Delta Q_{IXRD} \cdot \frac{\cos(\gamma - \beta)}{\cos(\beta)} + \Delta Q_x \cdot \tan(\beta) \tag{3.4}$$

$$\Delta Q_x \quad = -\Delta Q_{IXRD} \cdot \frac{\cos(\gamma - \beta)}{sin(\beta)} + \Delta Q_z \cdot \cot(\beta) \tag{3.5}$$

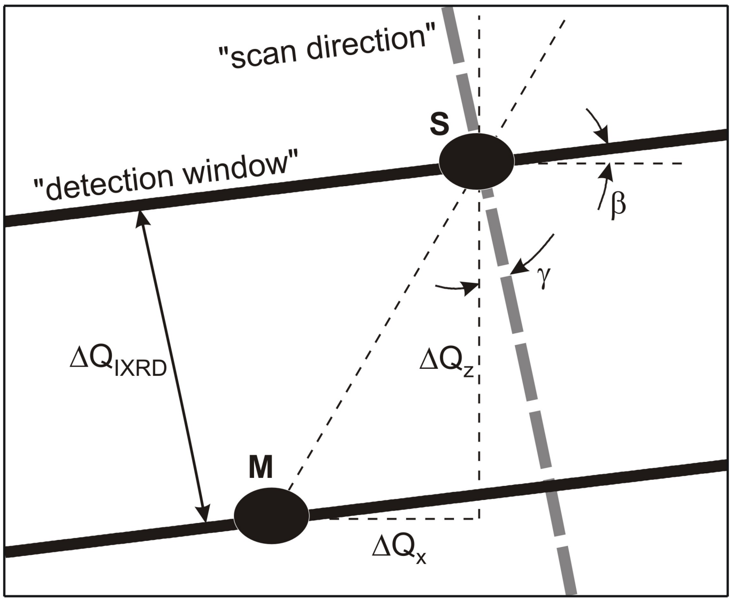

Figure 3.5: Sketch of reciprocal space for a crystalline structure. Points "S" and "M" are the centers of diffraction from "substrate crystal" and multilayer structure, respectively.

where β and γ are the angles given by:

$$\beta = \frac{\pi}{2} - \delta_{br}, \quad \gamma = \varepsilon_{br}$$

δ_{br} and ε_{br} are the incident and the detection angles for the exact Bragg diffraction of the "substrate crystal". From equations 3.4 - 3.5 it follows that the relation between the measured parameters ΔQ_{IXRD} and ΔQ_z, ΔQ_x depends on the incident and on the detection Bragg angles of the "substrate crystal". Therefore, for the "substrate crystal" the suitable reflections must be found depending on the required information. We analyze equations 3.4 - 3.5 for two important cases: 1) determination of the vertical lattice parameter and 2) determination of the lateral lattice parameter.

3.3.2 Determination of the vertical lattice parameter of crystalline structures

From relation 3.4 it follows that we need to consider two parameters. The first one is parameter $\cos(\gamma - \beta)/\cos\beta$ which describes the resolution of the setup for the vertical distance. In order to get optimized measurement conditions this parameter should be close or less than unity. Otherwise, the measured distance ΔQ_{IXRD} will be smaller than the distance ΔQ_z and the setup is not sensitive to small ΔQ_z, for example, in case of a small lattice mismatch between substrate and layer crystals. The second parameter is $tan\beta$ which describes how the reflection depends on the lateral distance ΔQ_x. If we have no information about this distance, i.e. information about the lateral lattice parameter of the structure, this parameter multiplied by the value of the lateral distance, gives the systematic error in the determination of the vertical lattice parameter. In order to decrease the systematic error, this parameter has to be close to zero or a symmetrical reflection which does not depend on the lateral lattice parameter should be used. Table 3.1 shows these two parameters and structure factor F for some reflections of h-GaN.

Table 3.1: Parameters $\cos(\gamma-\beta)/\cos\beta$, $tan\beta$ and structure factor F for some reflections of h-GaN

	$\cos(\gamma-\beta)/\cos(\beta)$	$\tan\beta$	F
($\bar{2}$024)	4.78	4.96	11.5
($\bar{1}\bar{1}$24)	5.22	5.21	24.5
(0002)	1.91	3.21	48.5
(20$\bar{2}$4)	0.95	−0.14	11.5
(11$\bar{2}$4)	**0.99**	**0.02**	**24.5**

Table 3.1 is not a full list of all possible reflections, here we intend to illustrate the most important reflections to understand the criteria for the choice of the reflection. The table shows that in case of asymmetrical reflections with small incident angles (reflections ($\bar{2}$024) and ($\bar{1}\bar{1}$24)) both parameters do not satisfy the requirements for the vertical mismatch determination. They have poor resolution for the ΔQ_z and depend strongly on the lateral mismatch. The symmetrical reflections for which the sensitivity to the lateral mismatch is not important (because in this case $\Delta Q_x = 0$) have a low resolution in ΔQ_z. After analyzing all possible reflections we conclude that the reflection with a large incident angle (11$\bar{2}$4) is most suitable for the determination of the vertical lattice parameter of structures grown on h-GaN. In table 3.2 we have summarized the suitable reflections of some "substrate crystals" for the determination of the vertical lattice parameter of multilayer structures.

Table 3.2: Suitable reflections of some "substrate crystals" for the determination of vertical lattice parameter of multilayer structures. Parameters $\cos(\gamma - \beta)/\cos\beta$, $tan\beta$ and structure factors F are shown.

"substrate crystal"	reflection	$\cos(\gamma-\beta)/\cos(\beta)$	$\tan\beta$	F
Si	(224)	1.02	0.19	55.8
GaAs	(135)	0.96	0.07	82.0
c-GaN	(224)	0.92	−0.03	59.7

3.3.3 Determination of the lateral lattice parameter of crystalline structures

For the determination of the lateral lattice parameter two parameters, namely, $\cos(\gamma - \beta)/\sin\beta$ and $\cot\beta$ are of importance. These parameters describe the resolution in Q_x-direction and the dependence of the chosen reflection on the vertical distance, respectively. We illustrate these two parameters and structure factor F for some reflections of h-GaN in table 3.3.

Table 3.3: Parameters $\cos(\gamma-\beta)/\sin\beta$, $cot\beta$ and structure factors F for some reflections of h-GaN.

	$\cos(\gamma-\beta)/\sin(\beta)$	$\cot\beta$	F
$(20\bar{2}4)$	−6.98	−7.32	11.5
$(11\bar{2}4)$	61.78	62.72	24.5
(0002)	0.59	0.31	48.5
$(\bar{2}024)$	0.96	0.20	11.5
$(\mathbf{\bar{1}\bar{1}24})$	**1.00**	**0.19**	**24.5**

The asymmetrical reflections with large incident angles which are well suited for the vertical lattice parameter determination are not appropriate for determination of the lateral lattice parameter. This means that it is not possible to use only one geometry of the IXRD for simultaneous determination of lattice parameters in both directions: parallel and perpendicular to the sample surface. From table 3.3 we see that the $(\bar{1}\bar{1}24)$ reflection is the most appropriate for the determination of lateral lattice parameter of a structure grown on h-GaN. In table 3.4 we have summarized the suitable reflections of some ”substrate crystals” for the determination of the lateral lattice parameter of multilayer structures.

Table 3.4: Suitable reflections of some ”substrate crystals” for the determination of vertical lattice parameter of multilayer structures. Parameters $\cos(\gamma-\beta)/\sin\beta$, $cot\beta$ and structure factors F are shown.

”substrate crystal”	reflection	$\cos(\gamma-\beta)/\sin(\beta)$	$\cot\beta$	F
Si	$(\bar{1}\bar{1}3)$	0.83	0.05	55.8
GaAs	$(\bar{1}\bar{1}3)$	0.82	0.03	119.8
c-GaN	$(\bar{1}\bar{3}3)$	0.99	0.02	58.7

4 Experimental setup of IXRD

4.1 Experimental setup for laboratory tests

The experimental setup of the IXRD for laboratory tests is schematically shown in figure 4.1. The main parts of the setup are X-ray tube, movable slit, Johansson monochromator, sample stage and multichannel detector.

The X-ray beams are generated by a Cu 2.2 kW ceramic tube which has the possibility to change between point and line focuses. For our experiments we have used line focus. The size of line focus is 0.4 mm in the scattering plane and 12 mm in direction perpendicular to the scattering plane. The controller type "PW3100/00" which consist of a generator (high tension tank and waterflow control) and electronics rack with CPU as well as the X-ray tube type "PW3373/00" have been produced and supplied by "Philips Analytical".

The X-radiation from the X-ray tube is monochromized and focused by the Johansson monochromator. We have applied a [111]-oriented Si monochromator crystal produced by INRAD (USA). The (333) reflection is used. The radius of the Rowland circle is 339 mm. Referring to equation 3.1 the distance between X-ray source and center of the monochromator and between center of the monochromator and center of the sample is 500 mm. The size of the monochromator is 50 mm (curved) x 15 mm (flat). As will be shown in the next section, the effective angular acceptance range of the monochromator is about two degrees.

The monochromatic X-beams are focused to the sample position as shown in figure 4.1. The use of a focused beam as well as of a multichannel detector allows to implement X-ray measurements without alignment of the samples and without positioning them during the measurements. Therefore the sample stage was constructed without goniometer. However, in order to realize conditions present in a MOCVD reactor, the sample holder has been equipped with a motor which allows to rotate the sample in azimuth direction.

For the collection of diffracted spectra we use the multichannel detector. The multi-

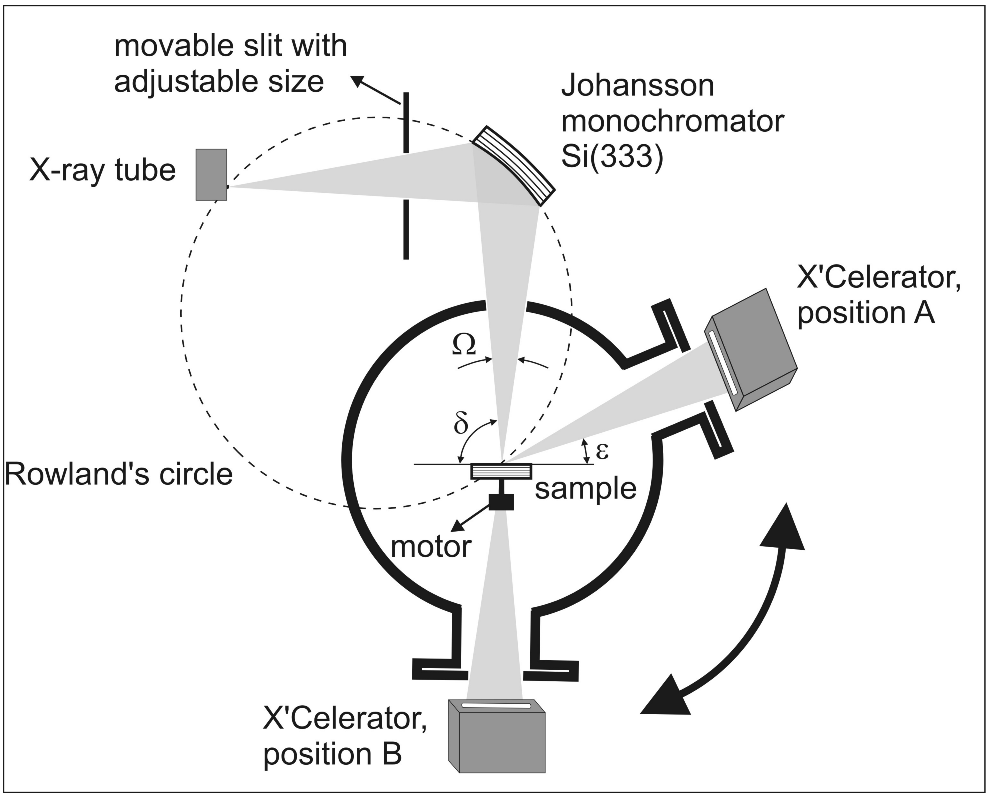

Figure 4.1: Experimental setup of the IXRD for measurements under laboratory conditions. The beams from the X-ray tube are monochromized and focused onto the sample. The diffracted beams are collected by the multichannel detector. The setup is additionally equipped with a movable slit in front of the monochromator and with a motor for azimuth rotation of the sample during measurement.

channel detector type ”PW3015/xx” X’Celerator was produced and supplied by ”Philips Analytical”. Following the product abbreviation of ”Philips Analytical” the detector will be called X’Celerator.

Figure 4.1 shows that the setup is designed in such a way that it is possible to install the X’Celerator in two positions. In position A the diffraction measurements can be performed. Position B is intended for the measurements of X-ray radiation coming directly from the Johansson monochromator. In the next section we use the position B of the X’Celerator for the investigation of diffractive and focusing properties of the Johansson monochromator.

Additionally, we have installed a movable slit in front of the monochromator. The movable slit equipped with a motion controller allows to perform fast measurements of reciprocal space maps as will be shown in chapter 5.1.

4.2 Test of the optical properties of the Johansson monochromator

The monochromatic and focused X-ray beams are provided by the Johansson monochromator. The efficiency of the whole setup is influenced by the quality of the monochromator. The production of the Johansson monochromator is complicated due to the bending radius of the crystal planes and the grinding radius of the crystal surface. Any deviations from the ideal parameters decrease the quality of the monochromator.

To investigate the properties of the monochromator we used the arrangement of the setup shown in figure 4.2. Using the narrow slit we pick up a narrow beam which incidents on the monochromator. By moving the narrow slit we cause an angular deviation of the

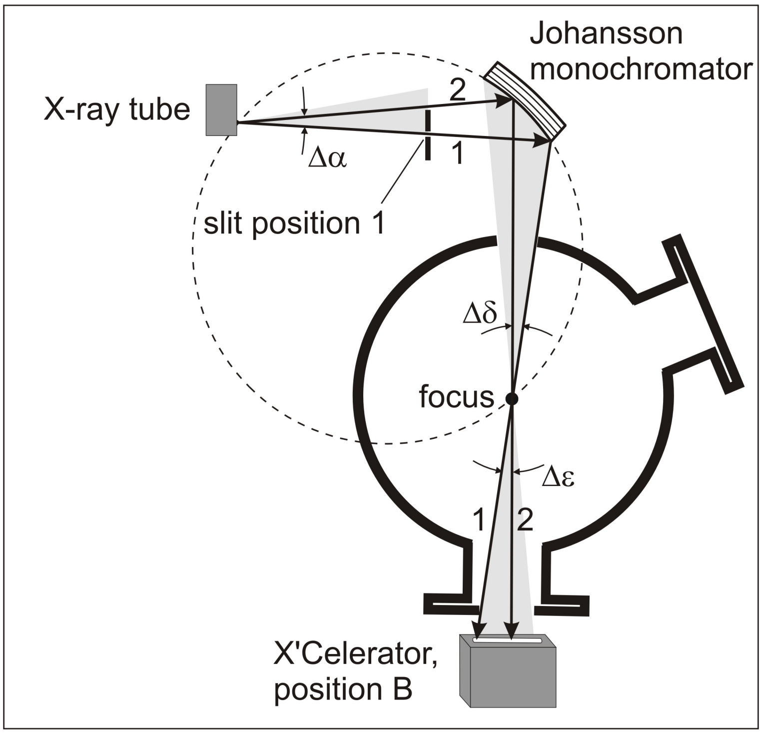

Figure 4.2: The arrangement of the setup for the investigation of optical properties of the Johansson monochromator. For each position of the movable slit the diffracted beams are measured with the X'Celerator at position B.

incident beam by the value $\Delta\alpha$ as is shown in figure 4.2 for two different beams 1 and 2 corresponding to two different slit positions.

After the reflection by the monochromator the beam is focused at the focusing point. The change of direction of the incident beam by angle $\Delta\alpha$ causes the angular deviation $\Delta\delta$ of the reflected beam at the focusing point. In case of a monochromator with perfect optical properties, the relative deviation of the reflected beam $\Delta\delta$ should be equal to the relative deviation of the incident beam $\Delta\alpha$.

The deviation of the reflected beam at the focusing point can be detected by the X'Celerator at position B as detection angle $\Delta\varepsilon$. The change in direction of the incident beam $\Delta\alpha$ can be calculated from the position of the movable slit.

Thus measuring the angular shift $\Delta\varepsilon$ of the diffracted beam for each position of the movable slit we can check the quality of the monochromator. The results of the measurements can be represented as a two-dimensional contour plot shown in figure 4.3 where the measured intensity is plotted versus the relative incident angle $\Delta\alpha$ and the relative detection angle $\Delta\varepsilon$. Zero value of the relative incident angle corresponds to the position of the beam at the middle of the monochromator. Zero value of the relative detection angle $\Delta\varepsilon$ is set to the maximum of the diffraction spectrum measured at $\Delta\alpha = 0$.

For the monochromator with perfect diffractive and focusing properties the scattered intensity should be uniformly distributed along the black line shown in figure 4.3. Figure 4.3 shows that there is a strong deviation of the direction of the diffracted beams from the ideal line as well as a decrease of the scattered intensity at both sides of the monochromator. The angular acceptance range of the monochromator is about two degrees which is less than four degrees specified by the producer of the crystal.

This can be also verified by the measurement of intensity diffracted by the Johansson monochromator without the slit. Figure 4.4 shows the distribution of intensity coming directly from the Johansson monochromator. The non-ideality of the monochromator causes the decrease of the active optical area of the monochromator and the variation of the reflected intensity by approximately a factor of two.

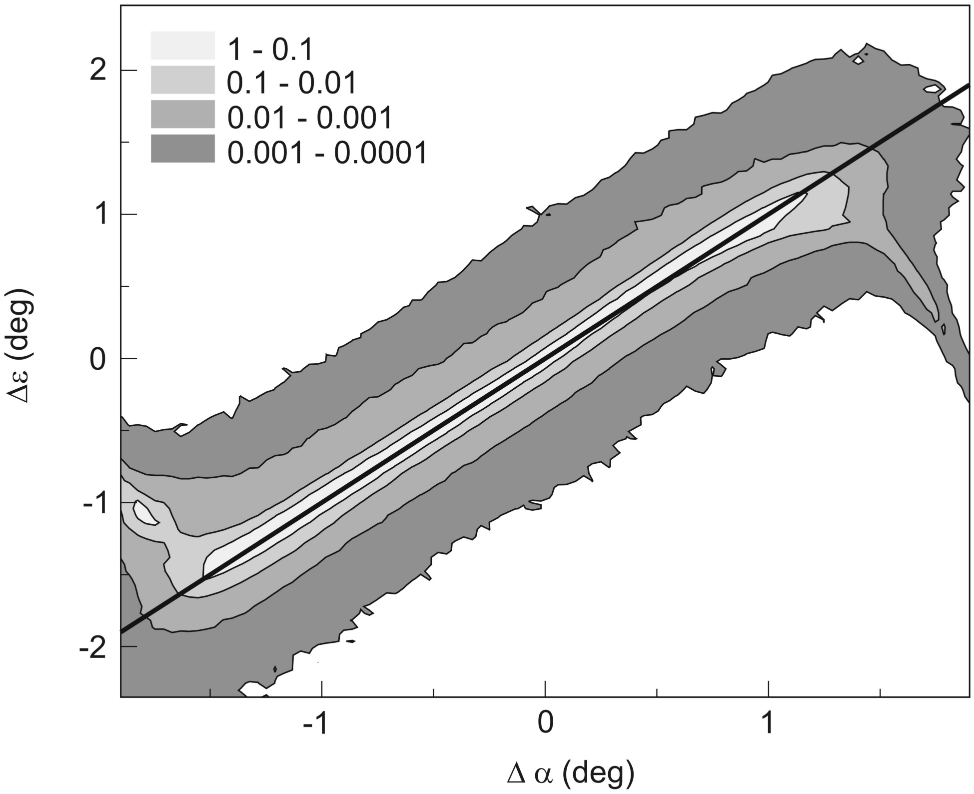

Figure 4.3: The distribution of intensity measured at different positions of narrow slit in front of the monochromator as a function of relative incident angle $\Delta\alpha$ and relative detection angle $\Delta\varepsilon$. There are deviations of the direction of the diffracted beams as well as the diffracted intensity from the ideal form at both sides of the monochromator.

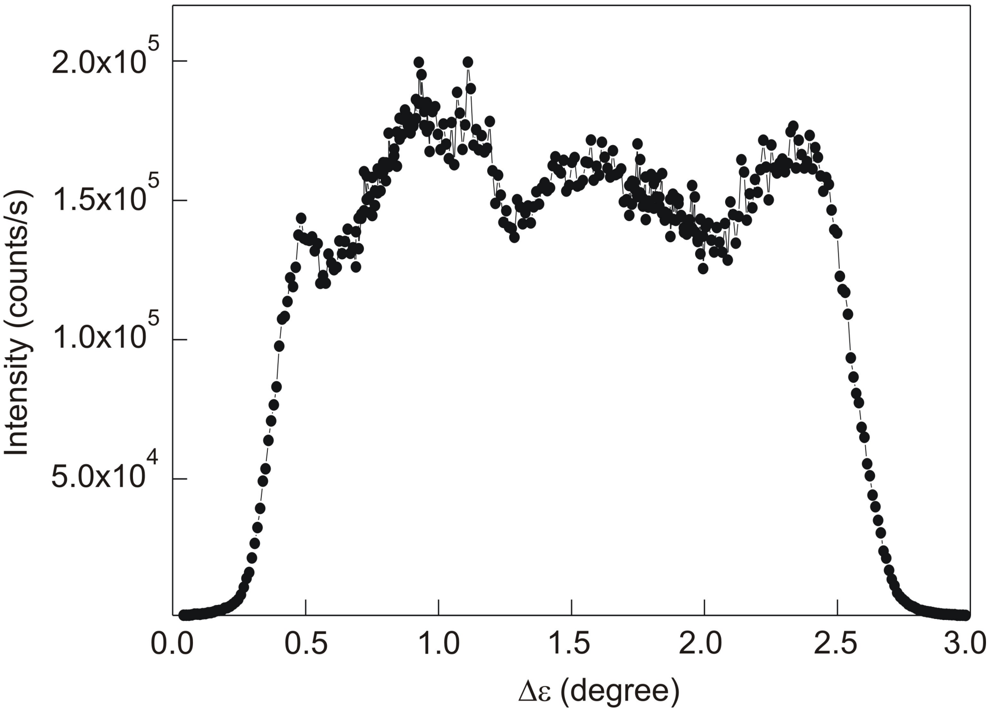

Figure 4.4: The intensity diffracted from the Johansson monochromator plotted versus relative detection angle $\Delta\varepsilon$. The imperfection of the monochromator causes the decrease of the active diffractive area of the monochromator and the variation of the diffracted intensity by approximately a factor two.

4.3 Performance test of the IXRD

In this section we describe the performance check of the IXRD. One way to do it is to compare the results of IXRD measurements with the measurements performed with a conventional high resolution diffractometer.

In section 3.2 we have explained the formation of IXRD spectra in reciprocal space. Referring to figure 3.4 we see that the measurement point in the IXRD setup can be obtained from the intensity distribution in reciprocal space (reciprocal space map) by summation of the intensity located within so-called "detection windows". The distance between different "detection windows" corresponding to different measurement points is determined by the distance between pixels of the detector. We have developed a procedure which allows to obtain a spectrum which is identical to that measured by the IXRD. The procedure is the following. The measurement point in the IXRD setup is performed at a certain detection angle ε. For this detection angle ε and a series of incident angles δ continuously varying between $\delta_{br} - \Omega/2$ and $\delta_{br} + \Omega/2$ (Ω is the angular aperture of the monochromator, δ_{br} is the incident angle under Bragg condition) we calculate the positions of points in reciprocal space located in the "detection windows" according to the expressions 3.2. For each measurement point we take into account the width of the "detection window" which is determined by the size of detector pixels in the scattering plane. Therefore in our procedure the detection angle ε is taken in the range between $\varepsilon - \varepsilon_d/2$ and $\varepsilon + \varepsilon_d/2$ where ε_d is the angular width of the detector pixels. After the summation of the intensities of reciprocal space points located within the "detection window" for each detection angle ε we obtain the spectrum which is identical to that measured by the IXRD setup.

In figure 4.5 the dots show the results of measurements with the IXRD setup from two different AlGaN/GaN heterostructures. The full lines are the curves extracted from reciprocal space maps using the procedure described above. The high resolution reciprocal space maps were measured on the Philips X'Pert-MRD diffractometer in triple axis mode using the hybrid monochromator with a primary beam divergence of 18-25 arc seconds. Figure 4.5 shows that there is good agreement between measured and extracted spectra so that we can conclude that the IXRD setup has a good performance.

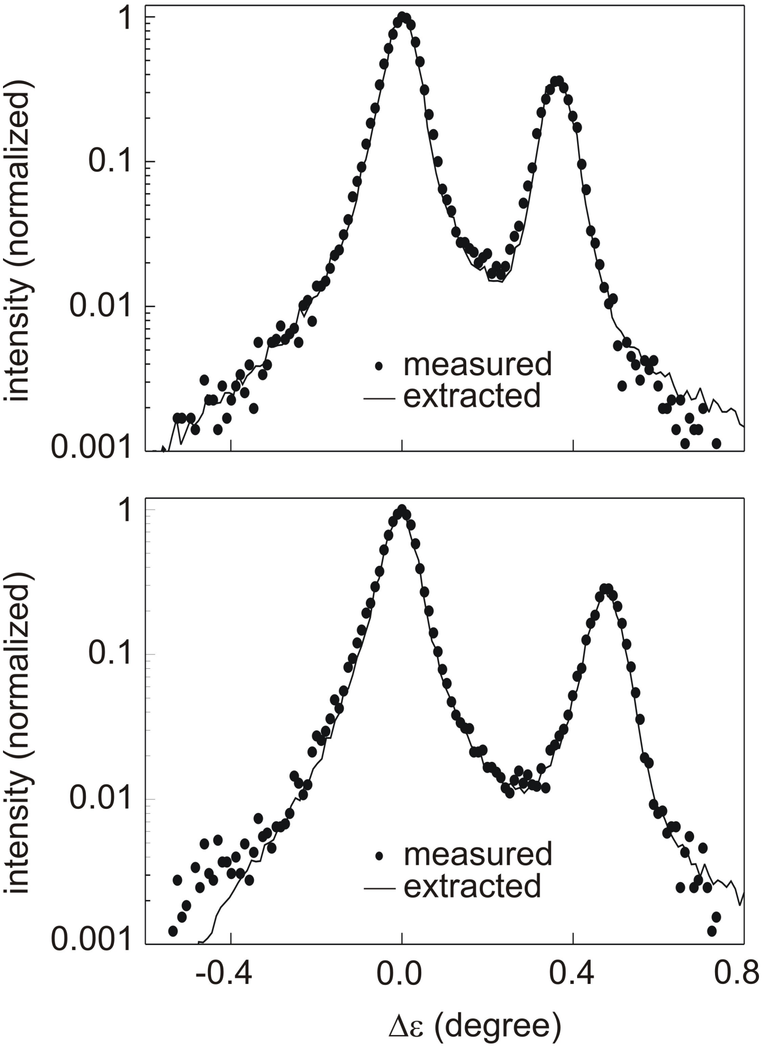

Figure 4.5: Comparison of spectra measured by the IXRD setup (dotted lines) and spectra extracted from reciprocal space maps (full lines). Two different AlGaN/GaN heterostructures with different Al content have been measured in a test of the IXRD.

5 Results of experiments under laboratory conditions

5.1 Use of the IXRD for fast ex situ characterization

5.1.1 Characterization of wurtzite AlGaN-, InGaN-based materials

In this section we focus on the potential of the IXRD for fast *ex situ* characterization of semiconductor multilayers. We concentrate mostly on the measurements of III-V nitride films which are wurtzite type AlGaN- and InGaN-based structures. Enormous progress in the development of wide-gap III-V nitride semiconductors (see for instance [27],[28]) has recently led to the commercial production of high-brightness light-emitting diodes. Therefore the structural characterization of these materials is highly demanded.

All tested multilayers are fully strained on the GaN layer so that only the vertical lattice parameter of the layers is of main interest. In case of strained ternary compounds the information about the vertical lattice parameter gives access to the chemical composition of the layers. Therefore all measurements with the IXRD setup were performed around the $(11\bar{2}4)$ reflection which is the most appropriate for analysis of the vertical features of the structures as described in section 3.3.

We have performed the first tests with two different AlGaN/GaN single heterostructures #1 and #2 which had different Al content. The vertical layer structure of both samples is the same and is schematically illustrated in figure 5.1.

In figure 5.2 at the left hand side we show the results of measurements performed with the IXRD setup for both samples. The diffractometer can clearly resolve both GaN and AlGaN peaks and provides the angular separation $\Delta\varepsilon$ of AlGaN and GaN diffraction peaks. The detailed description of the interpretation of measurement result is given in Appendix B. We depict the evaluated compositions of AlGaN layers in figure 5.2.

Figure 5.2 shows that the increase in the Al content of the AlGaN layer of about 4

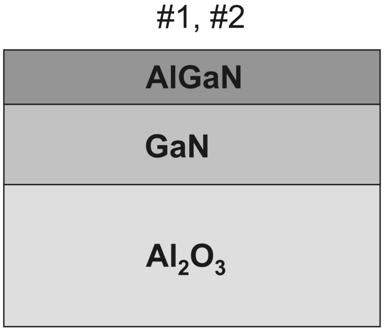

Figure 5.1: Sketch of the vertical layer structure of the single heterostructures #1 and #2.

percent leads to a considerable shifting of the AlGaN peak away from the substrate peak. The measurement time was 4 seconds for each sample.

For comparison we have performed measurements with the conventional high resolution equipment. The ω - 2Θ measurements are commonly used for the composition measurements of alloy semiconductors. The high resolution measurements were performed with the Philips X'Pert-MRD diffractometer in triple axis mode using the hybrid monochromator with a primary beam divergence of 18-25 arc seconds. In figure 5.2 at the right hand side we show ω - 2Θ scans from samples #1 and #2 around the (0002) reflection. The relative position of the AlGaN peak with respect to the substrate peak provide the chemical composition of both samples. The measurement time is considerably longer than for the IXRD setup and is about 30 minutes for each sample.

These results demonstrate that measurements with the IXRD setup give the same chemical composition of alloy semiconductors as the standard high resolution equipment. A slight change in Al composition can be clearly resolved by the IXRD setup. As a big advantage the IXRD setup offers significantly shorter measurement times (more than two orders of magnitude less than the standard equipment) and absence of alignment of the samples before measurements.

The next tests are measurements of two different multiple quantum wells (MQWs). The vertical structures of the investigated MQWs are schematically illustrated in figure 5.3. Samples #3 and #4 consist of 5 and 10 periods of InGaN (well) and GaN (barrier) layers, respectively. The samples have different periodicity (well thickness + thickness of barrier). They differ as well in the In content of the active InGaN layers. In figure 5.4 at the left hand side we illustrate the results of measurements with the IXRD. The X-ray patterns show clearly resolved zero- and first-order superlattice peaks. For our

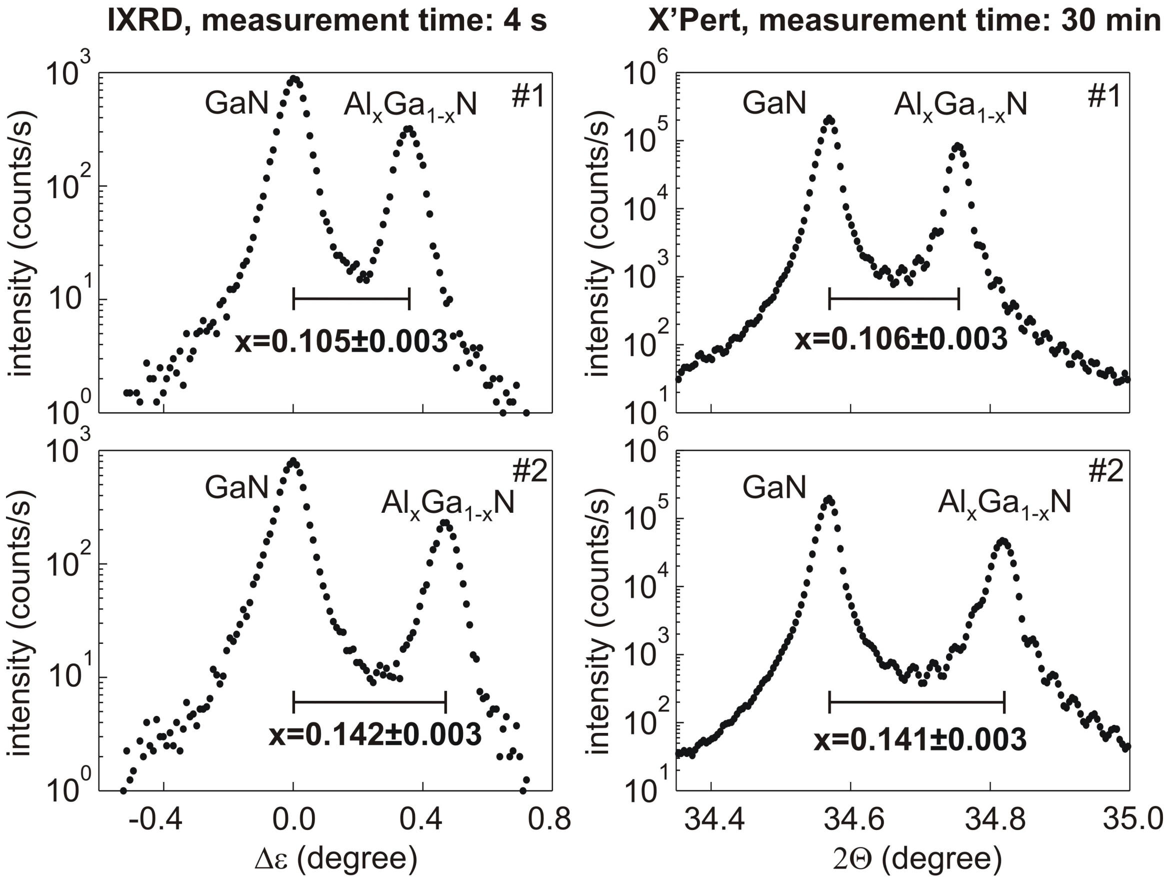

Figure 5.2: The spectra of single heterostructures #1 and #2 collected on the IXRD (at the left hand side) and measured on the standard high resolution equipment (at the right hand side). The information about the Al content is identical for both methods within experimental error. The time of measurement is significantly shorter for the IXRD.

IXRD setup it was not possible to observe higher order superlattice peaks, because the acceptance angle of the primary beam is only about two degrees. The measurement time was 40 seconds for each sample. The angular position of the zero-order superlattice peak corresponds to a lattice parameter determined by $(d_w c_w + d_b c_b)/(d_w + d_b)$ where d_w, c_w and d_b, c_b are the thicknesses and lattice parameters of the well and the barrier layers, respectively. Knowing the thicknesses of well and barrier layers from the growth conditions and the lattice parameter of the GaN layer we get the lattice parameter of the well layer, i.e., the information about the composition of the well layer. The relative position of neighboring peaks yield the information about the periodicity $D = d_w + d_b$ of the structure.

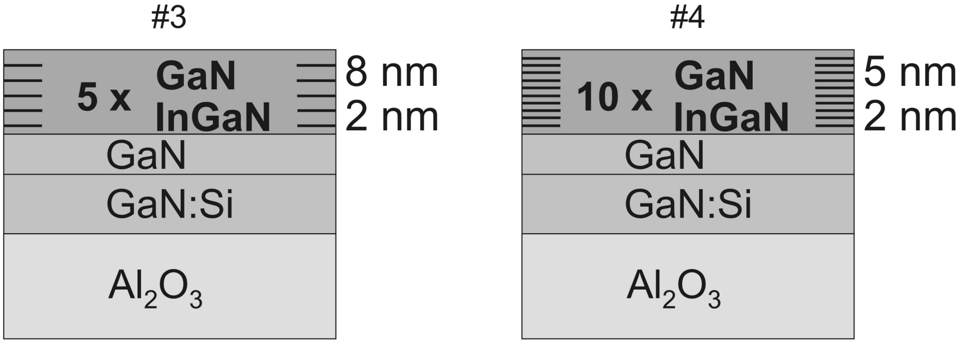

Figure 5.3: Schematic illustration of the vertical structures of tested multiple quantum wells.

In figure 5.2 at the right hand side we show the results of (0002) ω-2Θ scans of samples #3 and #4. Following the procedure of interpretation of such measurements [1] we determine the In content and the periodicity of the structures for both samples. There is an perfect agreement between the results obtained by the IXRD and by standard high resolution equipment.

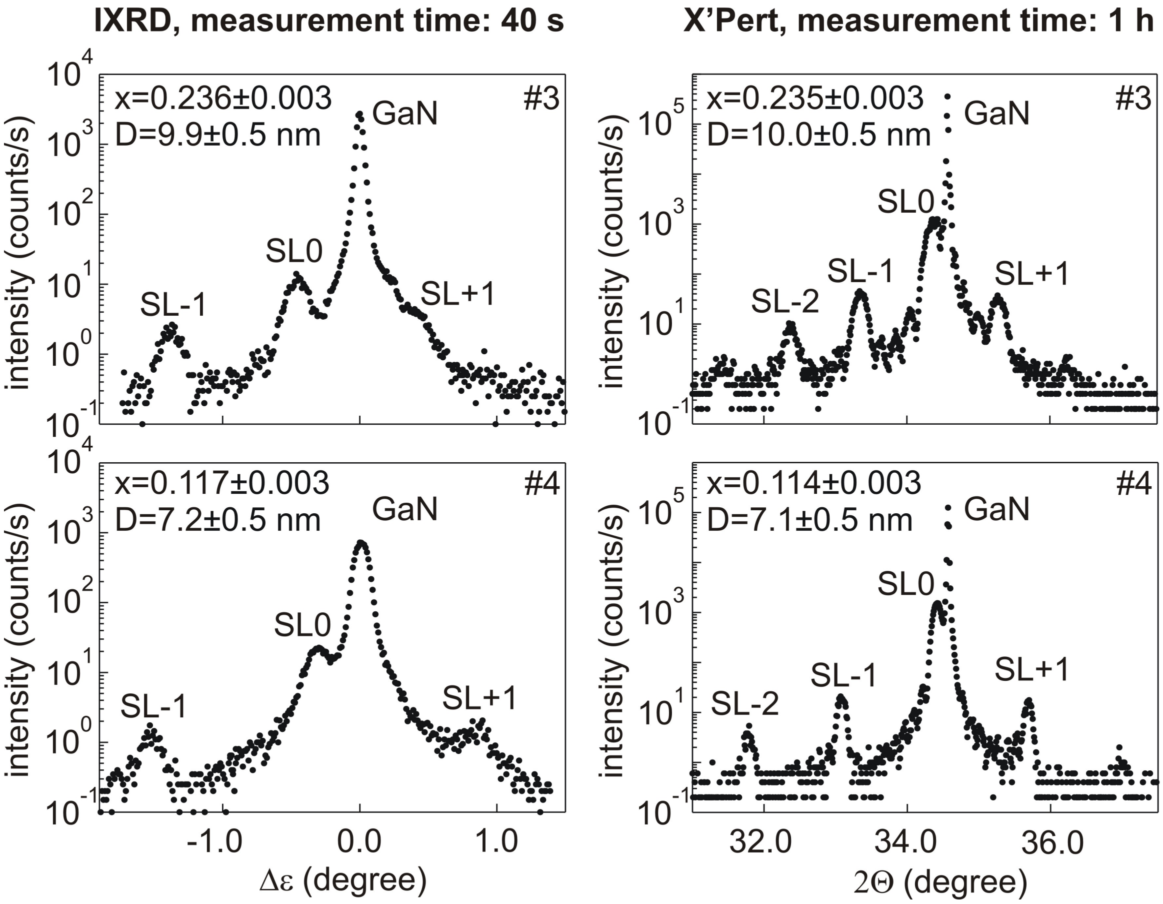

Figure 5.4: X-ray diffraction patterns of two different multiple quantum wells #3 and #4 measured by the IXRD are shown at the left hand side. The chemical composition of active InGaN layers and the periodicity of the structures were obtained from the angular position of the zero-order peak and relative position of neighboring superlattice peaks. For comparison at the right hand side we show $\omega - 2\theta$ scans measured by the high resolution equipment.

5.1.2 Measurements on SiGe

It is likely that SiGe will form the basis of high speed transistor devices. Due to the successful and rapid development of the growth technology, SiGe structures exhibit very sharp peaks in X-ray diffraction spectra and X-ray characterization of these materials usually demand advanced high resolution technique. The question is what is the potential of the IXRD for fast post-growth characterization of this industrially important material system. In figure 5.5 we show the sketch of a sample which consists of a $Si_{1-x}Ge_x$ alloy layer grown on a bulk Si substrate (sample #5).

Figure 5.5: Schematic illustration of the vertical structure of sample #5.

The left side of figure 5.6 shows the (224) diffraction spectrum measured with the IXRD. The IXRD allows to resolve the diffraction peak of SiGe alloy which can be clearly separated from the Si diffraction peak. The angular distance between $Si_{1-x}Ge_x$ and Si reflection peaks provides the composition x following the procedure described in Appendix B. Beside the main $Si_{1-x}Ge_x$ and Si diffraction peaks the IXRD diffraction pattern exhibits interference fringes (or Pendellösung fringes). This phenomenon is similar to the diffraction pattern of light falling on a narrow slit (details see for instance in [1] or [24]). The angular distance between fringes is directly connected to the thickness of $Si_{1-x}Ge_x$ alloy. We show the evaluation of the thickness of the epilayer in Appendix B.

Both parameters, the composition x and thickness d gathered from X-ray pattern are shown in figure 5.6. The additional diffraction peak at the right side of the Si peak results from the diffraction of the $K\alpha_2$ line which is presented in the beams reflected from the Johansson monochromator.

The right side of figure 5.6 shows the (004) $\omega - 2\Theta$ scan measured by the X'pert MRD diffractometer. The simulation of X-ray pattern performed by the dynamical theory of X-ray diffraction gives the composition x and thickness d of the $Si_{1-x}Ge_x$ layer.

Beside the fact that the results obtained by the IXRD and by the X'Pert MRD diffractometer are identical, the IXRD offers significantly shorter data collection time.

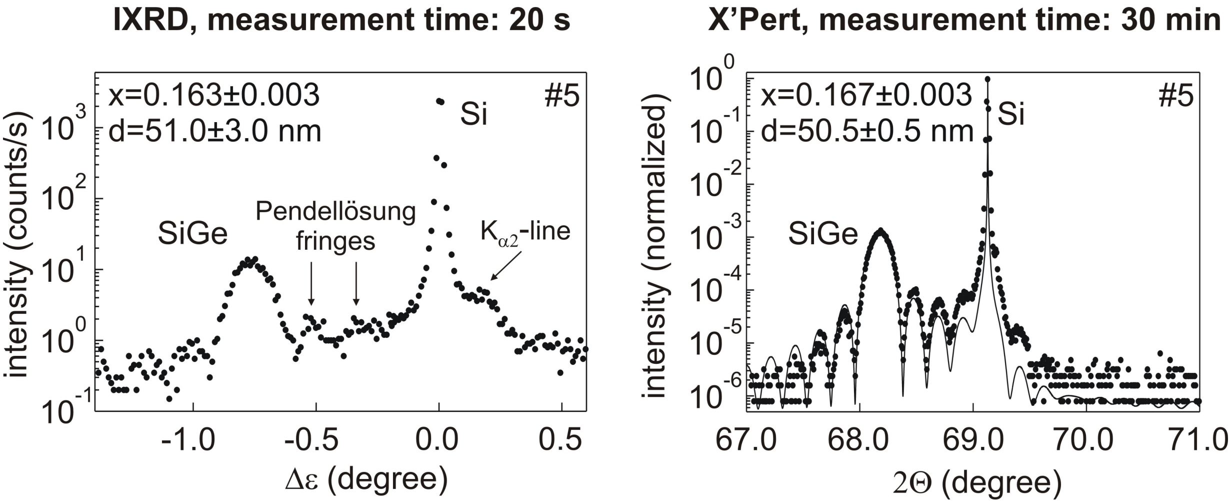

Figure 5.6: Left side of the picture shows the (224) diffraction scan of $Si_{1-x}Ge_x$ alloy grown on the Si substrate measured by the IXRD. The substrate and alloy peaks as well as interference fringes are clearly resolved and provide composition x and thickness d of the layer. For comparison the (004) X-ray diffraction pattern and theoretical curve (full line) are shown at the right hand side of the picture.

5.1.3 Fast reciprocal space mapping

A more comprehensive analysis of the structural properties can be performed by X-ray diffraction reciprocal space mapping. Reciprocal space mapping is the collection of scattered intensity around the reciprocal lattice points of layered structures, and it is usually performed by series of diffractometer scans. The resulting reciprocal space map (RSM) represents the contours of constant scattered intensity as a function of reciprocal space coordinates. The RSMs offer information about the status of strain and the structural quality of semiconductor multilayers which is not obtainable in ω - 2Θ measurements [2]. However, the use of the standard X-ray equipment for the measurement of RSMs demands long data collection times which are in the order of several hours. Our IXRD allows to measure a RSM in several minutes. The measurement procedure is explained in figure 5.7.

By moving the narrow slit in front of the monochromator we change the angle of incidence of monochromatic X-rays onto the sample as shown in figure 5.7 for two different positions 1 and 2 of the slit. Collecting the diffracted beams by the X'Celerator for different positions of the slit we simultaneously vary both the incident angle δ and the

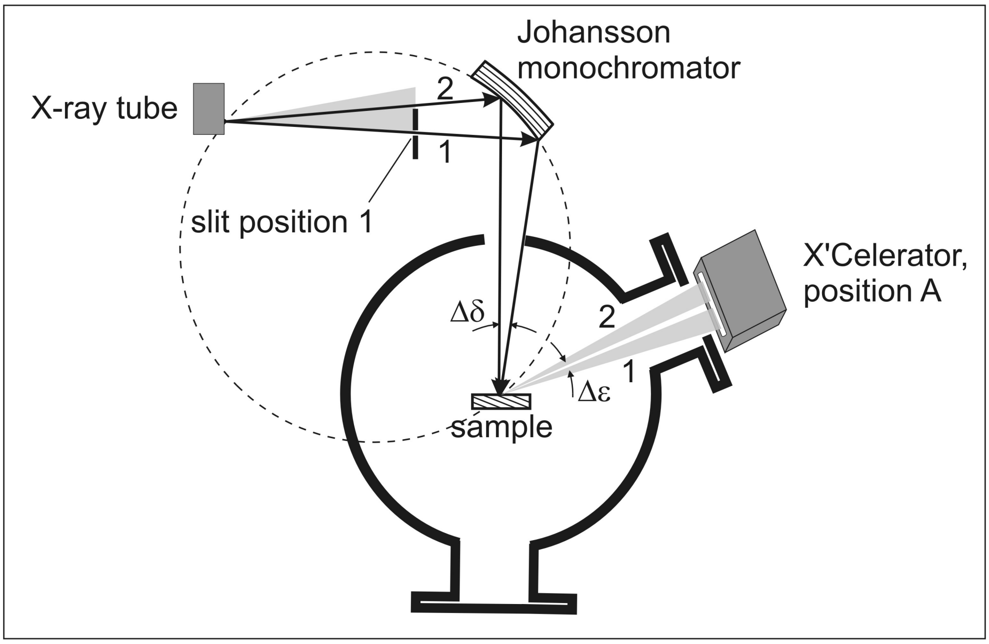

Figure 5.7: The procedure of reciprocal space mapping with the IXRD. By moving the narrow slit in front of the monochromator and by collecting the diffracted spectra by a multichannel detector at different detection angle ε we collect the distribution of intensity in reciprocal space.

detection angle ε. The intensity of the diffracted X-ray radiation is then represented as a function of reciprocal space coordinates which are calculated from incident and detection angles according to equations 3.2.

In figure 5.8 we show $(11\bar{2}4)$ reciprocal space maps measured by the IXRD setup (at the left hand side) and by the high resolution diffractometer (at the right hand side) of the single heterostructures #1 and #2. The standard high resolution RSMs were derived from a series of 2Θ scans performed at different ω angles. The dashed lines show the calculated locations of fully strained and fully relaxed AlGaN layers of varying Al content. From figure 5.8 it is obvious what potential is offered for immediate identification of the strain status of structures by reciprocal space mapping. Both IXRD and the high resolution diffractometer give the same positions of the Bragg reflexes in reciprocal space and provide identical compositions of the fully strained layers.

In figure 5.9 we illustrate the reciprocal space maps of the multiple quantum wells #3 and #4 measured by the IXRD setup (at the left right hand) and by the standard high resolution diffractometer (at the left right hand). The superlattice reflections are clearly observed with both methods. The dashed lines show the calculated locations of the fully

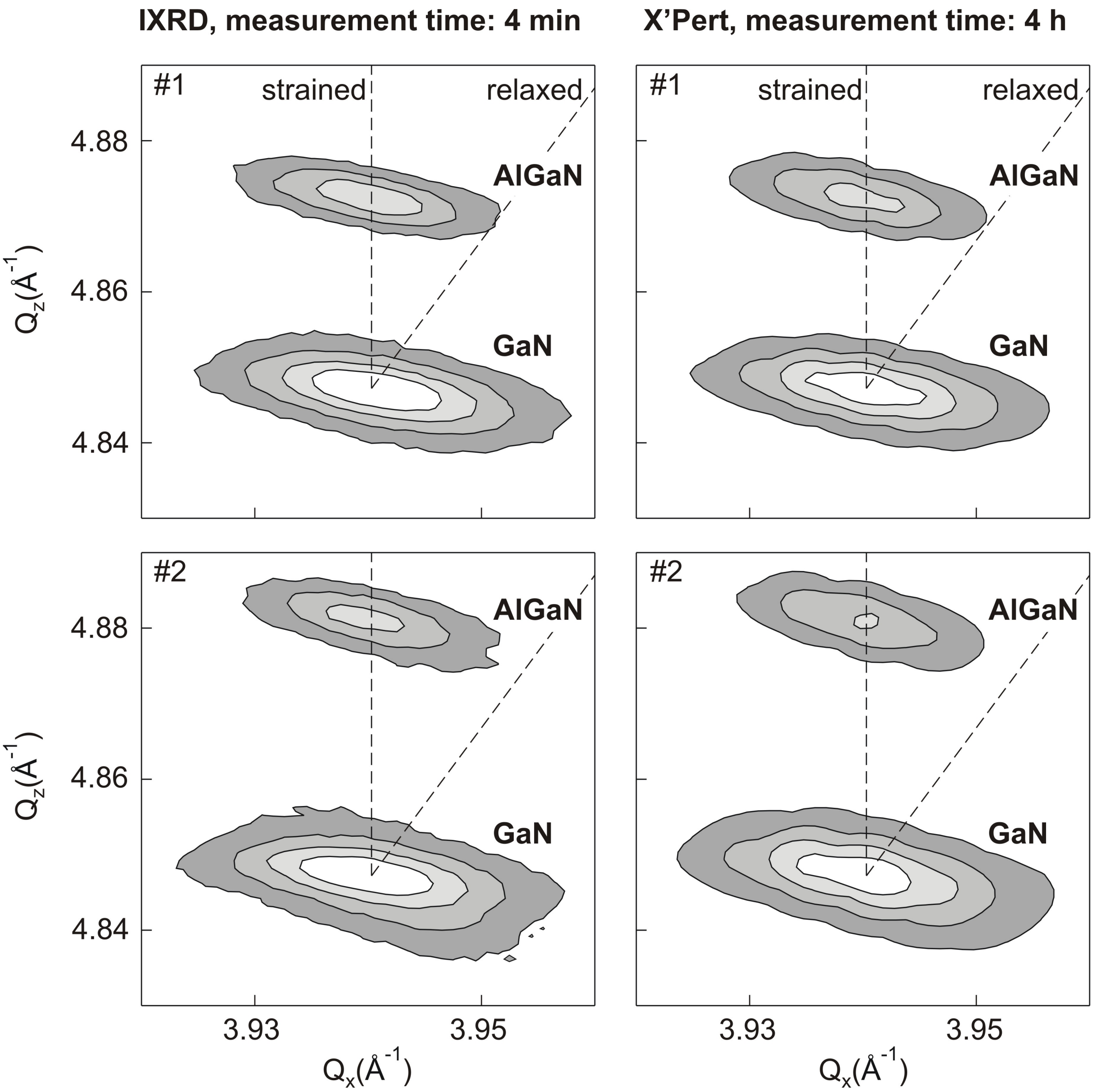

Figure 5.8: The $(11\bar{2}4)$ contours of constant scattered intensity of single heterostructures #1 and #2 measured by IXRD (at the left side) and collected on the high resolution diffractometer (at the right side) are shown. The iso-intensity contours correspond to 0.5, 0.25, 0.1, 0.03 of the maximal diffracted intensity. The information about strain state and the composition of alloys are the same whereas the measurement time for IXRD setup is considerably shorter.

strained and the fully relaxed InGaN layers of varying In content. In this case the strain status, In content of active layer and the periodicity of the structures are obtained.

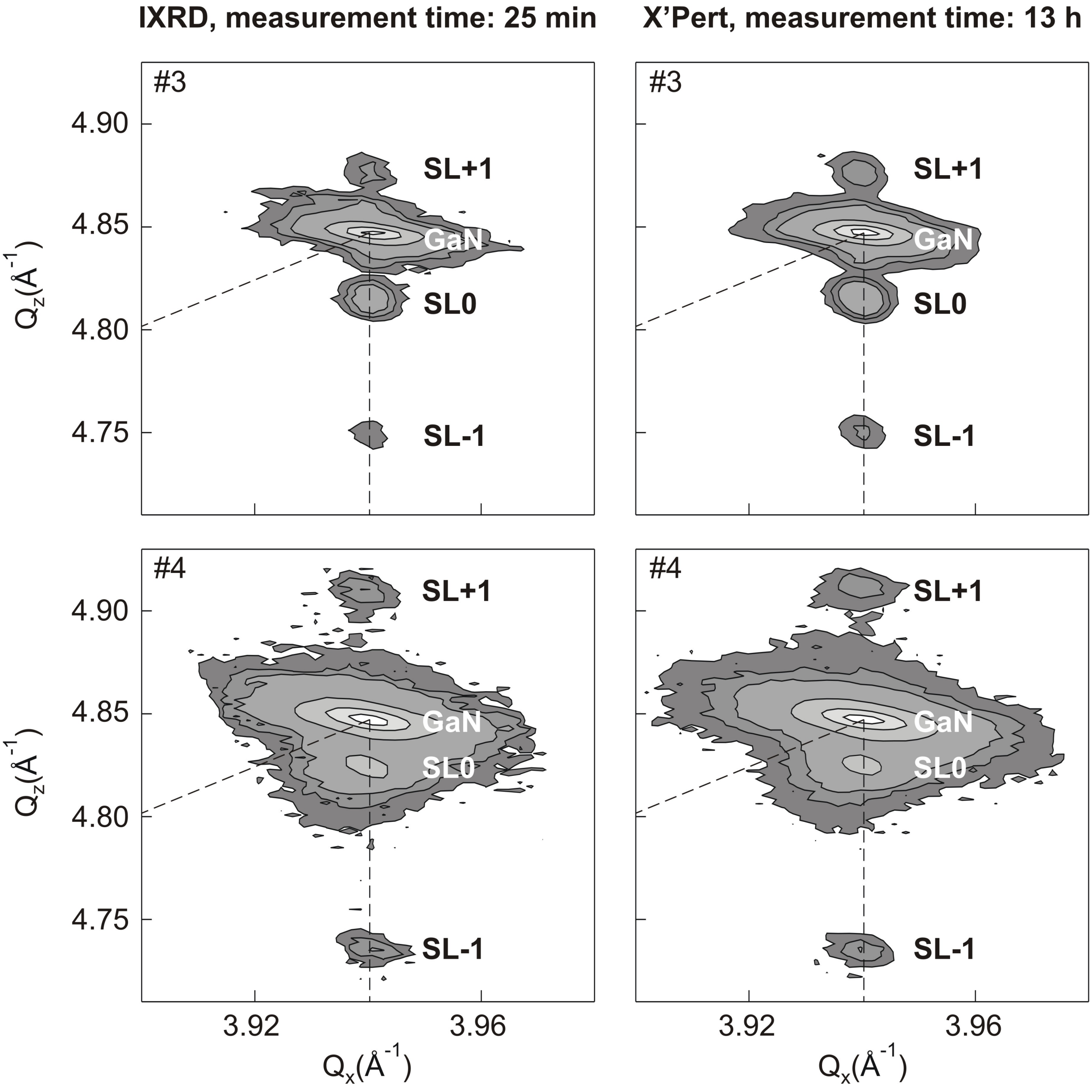

Figure 5.9: The reciprocal space maps from multiple quantum wells #3 and #4 measured by the IXRD (at the left hand side) and by X'Pert MRD diffractometer (at the right hand side) are shown. The iso-intensity contours correspond to 0.5, 0.1, 0.01, 0.001, 0.0005, 0.0002 of the maximal diffracted intensity. The results of reciprocal space mapping performed by the X'Pert MRD diffractometer are consistent with those obtained by the IXRD.

In figure 5.10 we illustrate the (224) reciprocal space maps of $Si_{1-x}Ge_x$ alloy #5 measured by the IXRD (at the left side of the picture) and by the X'Pert MRD diffractometer (at the right side of the picture). In contrast to the RSM measured by the X'pert MRD diffractometer the reciprocal space map collected on the IXRD exhibits a significant broadening of the main Si and $Si_{1-x}Ge_x$ reflexes as well as of the reflexes due to interference. There are several reasons for this broadening: i) Due to the use of the narrow slit in front of the monochromator we can not obtain an ideal parallel beam. For our experiments we have used a slit of 0.2 mm width. Geometrical estimations show that in this case the divergence of the primary beam is about 92 arc seconds. The X'Pert MRD diffractometer has a divergence of the primary beam of only 18-25 arc seconds. This divergence is responsible for the broadening of reflexes along the Q_x axis. ii) The finite size of the source of 0.4 mm in the scattering plane reduces the instrumental resolution $\Delta\lambda/\lambda$ of the IXRD. X-rays emitted from the source which have incidence angles different from the exact Bragg angle are still reflected by the Johansson monochromator but at another wavelength. Due to this fact the IXRD has lower instrumental resolution than the high resolution diffractometer as has been shown in [29]. The presence of a $K\alpha_2$-line in IXRD spectrum can not be excluded. iii) The angular resolution of the IXRD in the "scan direction" is limited by the size of the detector pixels and by the distance between the sample and the detector. In the IXRD the angular resolution is about 36 arc seconds which is less than in the case of the high resolution diffractometer which in triple axis configuration has a resolution of 12 arc seconds. The reduced resolution causes additional broadening in the "scan direction" which is almost parallel to the Q_z axis.

This makes the IXRD less suitable for a detailed analysis of the intensity distribution around reciprocal space lattice points of layered structures with high crystalline perfection like SiGe/Si or AlGaAs/GaAs. However, the positions of the reflections in IXRD measurement are consistent with those obtained by the X'Pert MRD diffractometer so that the structural information on composition, thickness and strain of the epilayers is identical.

From the series of measurements described in this subsection we can conclude that the IXRD can perform reciprocal space mapping in significantly shorter times than a standard X-ray diffractometer. The structural information on composition, thickness and strain obtained by the IXRD and X'pert diffractometer is identical within the experimental error.

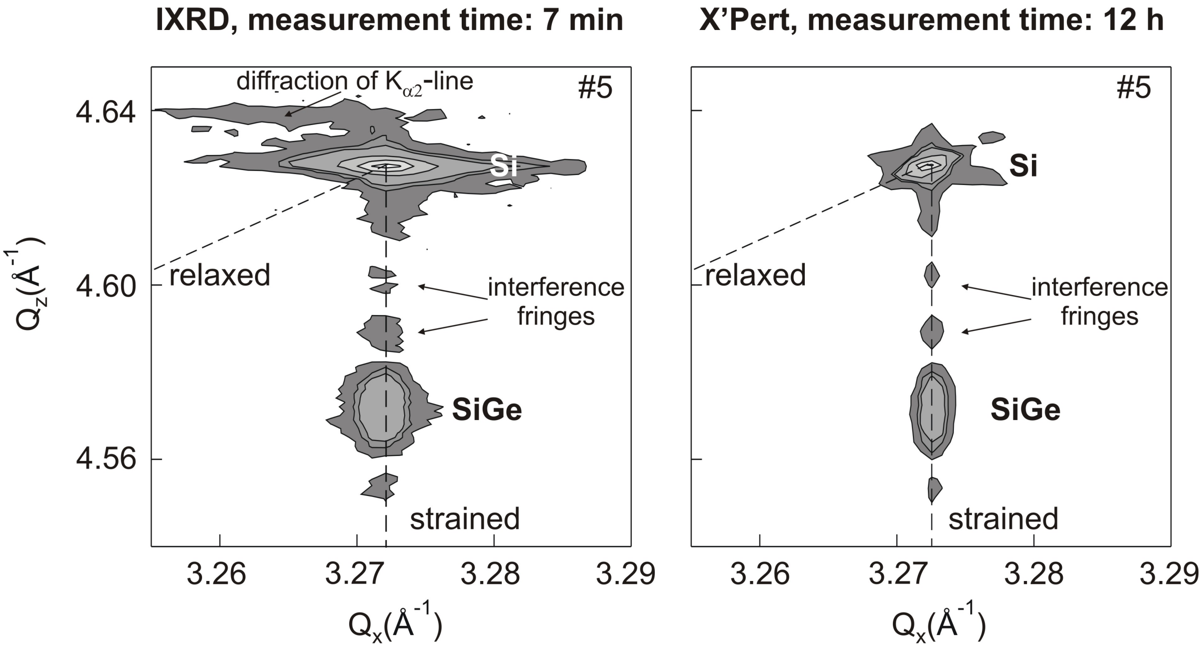

Figure 5.10: The reciprocal space maps of SiGe/Si collected by the IXRD and by X'Pert MRD diffractometer. The iso-intensity contours corresponding to 0.5, 0.1, 0.01, 0.001, 0.0005, 0.0001 of the maximal diffracted intensity are shown. The required information on the strain status, composition and thickness of the alloy is identical for both methods.

5.2 Measurements under conditions in a MOCVD reactor

5.2.1 Measurement conditions and principles of data collection

In this section we describe the abilities of the IXRD for X-ray analysis of crystalline layers under conditions similar to that in a MOCVD reactor. The MOCVD growth process is accompanied by a rotation of the sample in a gas flow. Furthermore, the gas flow can cause a wobble of the sample around the rotation axis. The rotation and wobble during growth are the most critical points for the *in situ* X-ray setup, because it can lead to a deviation of the sample from an angular condition of diffraction and to a reduction of the diffracted X-ray intensity. In our experiments we have realized the conditions met in the MOCVD growth reactor Aixtron. In this growth reactor the rotation speed depends on the flow rate and can be different for different growth modes. However, in average the rotation speed is about 1 rotation per second, possible fluctuations are not significant and can be easily taken into account by the measuring procedure of the IXRD. To clarify the situation regarding the wobble of the samples, we measured the deflection of a laser beam during MOCVD growth and found out that the wobble of the sample induces an angular deviation of the sample rotation axis of about 0.3 degree at maximum.

To simulate these conditions in the laboratory we have equipped the sample stage of our IXRD setup with an electrical motor which allows to rotate the sample with the rotation speed of 1 rotation per second. A misalignment of the rotation axis leads to a wobble of the sample by 0.7 degree at maximum. Thus, we have realized the same conditions as the conditions present in the real MOCVD growth system.

The use of a focused beam and the multichannel detector in the IXRD setup allows to get diffraction conditions and to collect the spectra even if a sample deviates from the exact Bragg condition. We have developed a measurement procedure which allows to collect X-ray data from rotating and wobbling samples.

In figure 5.11 we demonstrate the principle of data collection from rotating and wobbling single heterostructure #1. A multichannel detector collects one X-ray spectrum within a time interval of 0.15 sec. This time corresponds to the time between two reflections from different azimuth positions of the wurtzite type crystal ((hhil) diffractions in the wurtzite type structures can occur at six different azimuth positions). Taking several spectra and shifting the maximum of each spectrum to the same position and adding all spectra together results in the pattern shown in figure 5.11 at the right hand side. The total measuring time is about 90 sec and exceeds the expected time of 15 sec (equals 100 times 0.15 sec) because of the time needed to transfer the data between the detector interface board and the computer.

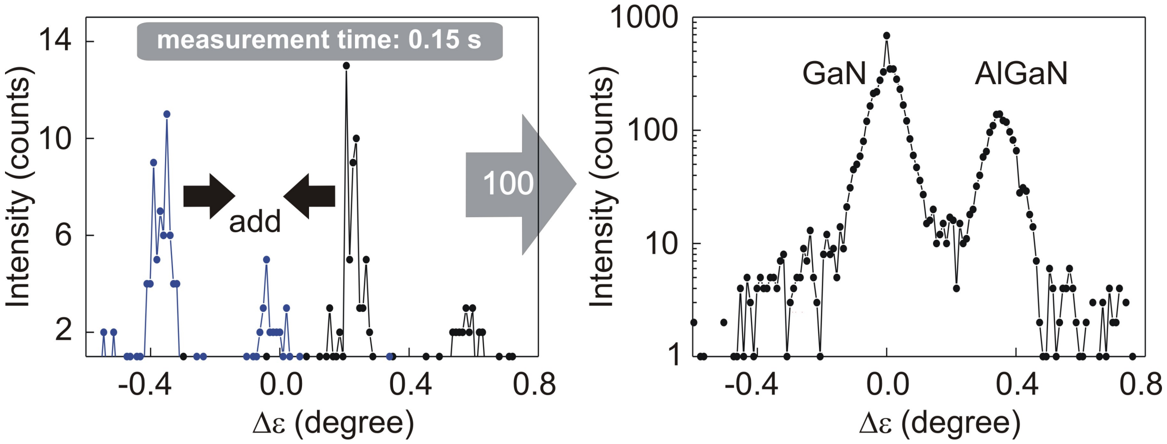

Figure 5.11: The principle of X-ray measurement from rotating and wobbling samples. Single shot spectra which are shifted to the maximum peak position are added. The result is depicted on the right hand side.

5.2.2 Results of measurements. Detection and resolution limits of the IXRD

In order to analyze the potentials of the IXRD for the X-ray analysis under conditions in a MOCVD reactor, we have performed X-ray measurements of different InGaN and AlGaN layers grown on GaN. Our aim is to find out the abilities and restrictions of the IXRD for X-ray analysis of rotating and wobbling samples.

The left hand side of figure 5.12 shows the $(11\bar{2}4)$ diffraction patterns taken on the IXRD of samples #6 and #7 which are InGaN and AlGaN layers grown on GaN, respectively. Each X-ray spectrum was obtained by collecting and adding 100 single shot scans and the total collection time was 90 seconds.

In order to find the accurate positions of the alloy (InGaN or AlGaN) and the GaN peaks, we have fitted each measured profile with two Pseudo-Voigt functions. The Pseudo-Voigt functions for GaN and alloy peaks as well as the total fits are plotted in figure 5.12 as full lines. The fits allow to obtain the relative angular positions $\Delta\varepsilon$ of alloy peaks in respect to the GaN peak. Using the procedure of composition determination described in Appendix B for the case of non-rotating layers, we get the In and Al contents of layers which are indicated in figure 5.12.

At the right side of figure 5.12 we plot the (0002) $\omega - 2\Theta$ scans of samples #6 and #7 measured with the high resolution diffractometer X'Pert MRD. The full lines are the calculations performed by means of the dynamical theory of X-ray diffraction. The

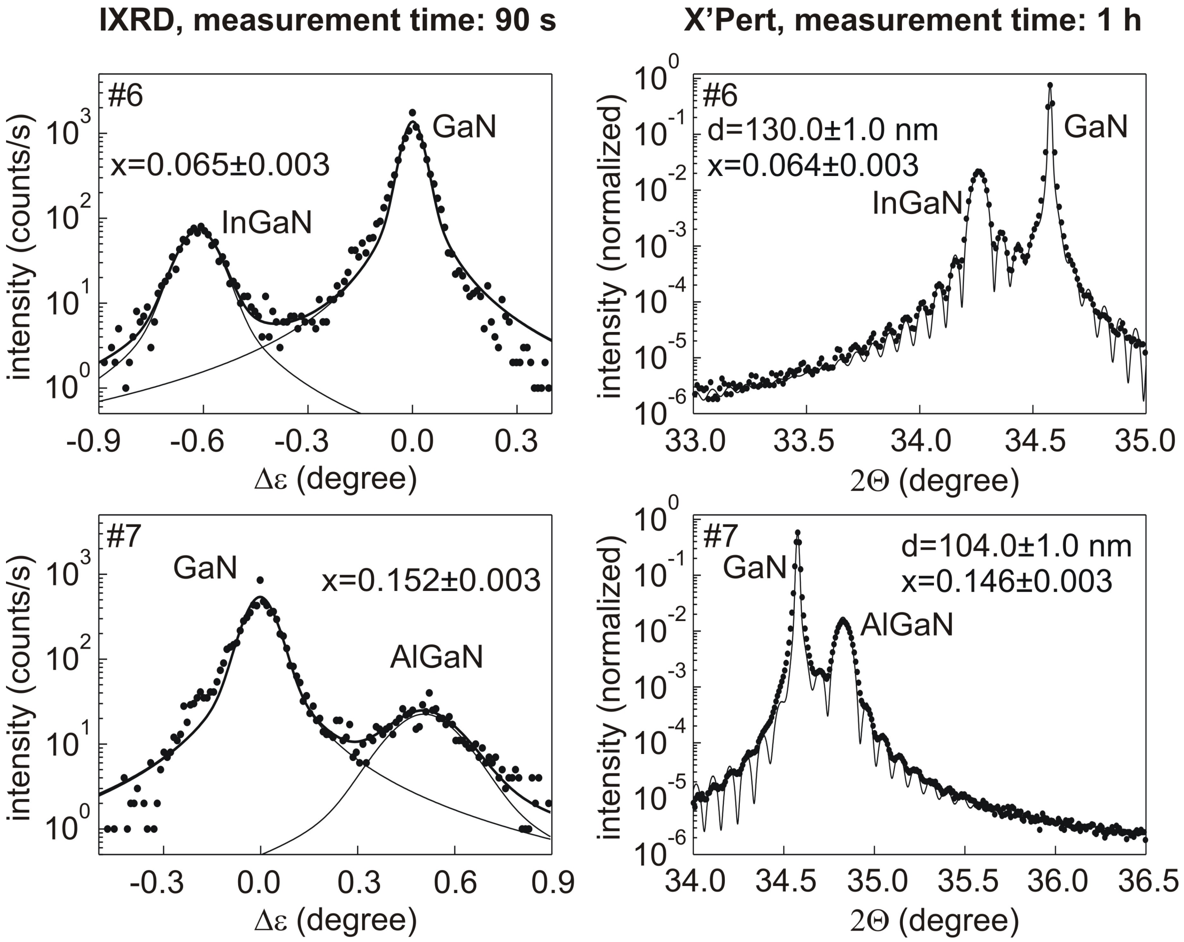

Figure 5.12: At the left hand side the X-ray spectra measured by the IXRD from rotating and wobbling InGaN/GaN and AlGaN/GaN samples are shown. The information about the chemical composition of the layers is obtained. (0002) $\omega - 2\Theta$ measurements of the samples performed by standard high resolution equipment and dynamical calculations shown at the right hand side provide accurate thickness d and composition x of the layers.

theoretical simulations provide accurate chemical compositions and thicknesses of InGaN and AlGaN layers. The collection time for (0002) $\omega - 2\Theta$ was one hour for each sample.

The results of the tests indicated in figure 5.12 demonstrate that the IXRD provides accurate information about the chemical composition of InGaN and AlGaN layers even when the samples are rotating and wobbling during measurement. The measurement time of 90 seconds corresponds approximately to the MOCVD of a 10 nm thick layer so that under real growth conditions the IXRD averages structural information with a resolution of about 10 nm.

Figure 5.13 depicts the spectra measured by the IXRD (at the left hand side) and by the X'Pert MRD diffractometer (at the right hand side) from samples #8 and #9 which had the thinnest InGaN and AlGaN layers measured in our tests.

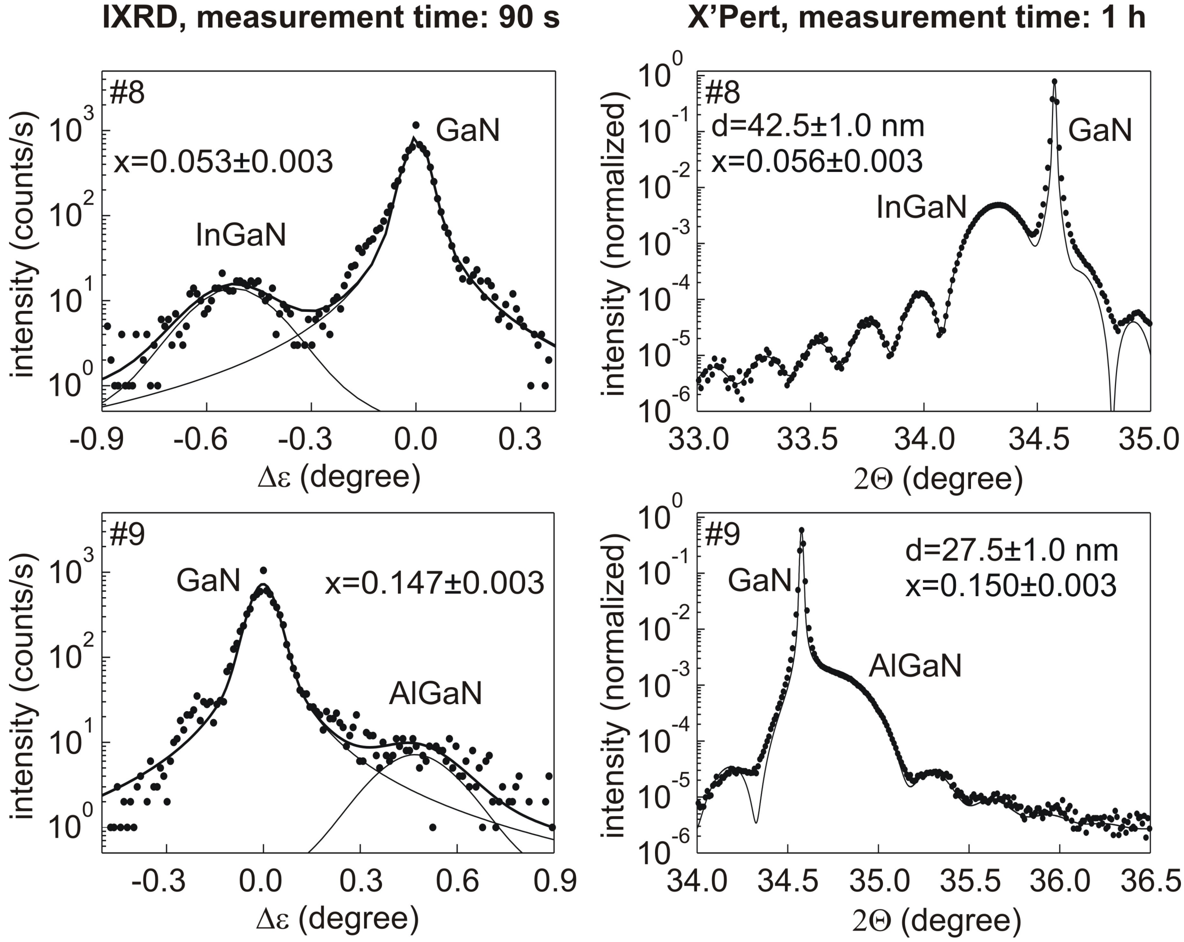

Figure 5.13: The spectra collected by the IXRD (at the right hand side) and by the X'Pert MRD (at the left hand side) from thin InGaN and AlGaN layers grown on GaN. The IXRD is able to implement X-ray measurements from 42.5 and 27.5 nm thick InGaN and AlGaN layers.

From the measurements with the IXRD setup we can draw two main conclusions. i) if we compare the measurement results of samples #8, #9 with the X-ray patterns of samples #6, #7, we see that the thickness of the alloy strongly influences the width of the diffraction peak, namely, the decrease of the layer thickness causes the broadening of the alloy peak. This finite broadening of the diffraction peaks is in a first approximation proportional to the inverse layer thickness [1], [24].

In figure 5.14 the full width at half maximum (FWHM) of all investigated AlGaN and

InGaN diffraction peaks is plotted versus the inverse layer thickness. The plot shows a linear dependence of the FWHMs of the diffraction peaks on the inverse layer thickness. Thus linear dependence of FWHMs of diffraction peaks on the thickness can be used for the determination of the relative increase of the thickness during growth, i.e. for the measurement of the growth rate. The interesting point to note is that the extrapolation of the curve to the values corresponding to the infinite thick layers results in a FWHM which equals to that of GaN measured with our IXRD setup. This means that the broadening of diffraction peaks of alloys due to imperfections is the same as in thick GaN. On the other hand the quality of GaN buffers predefines the quality of the alloys.

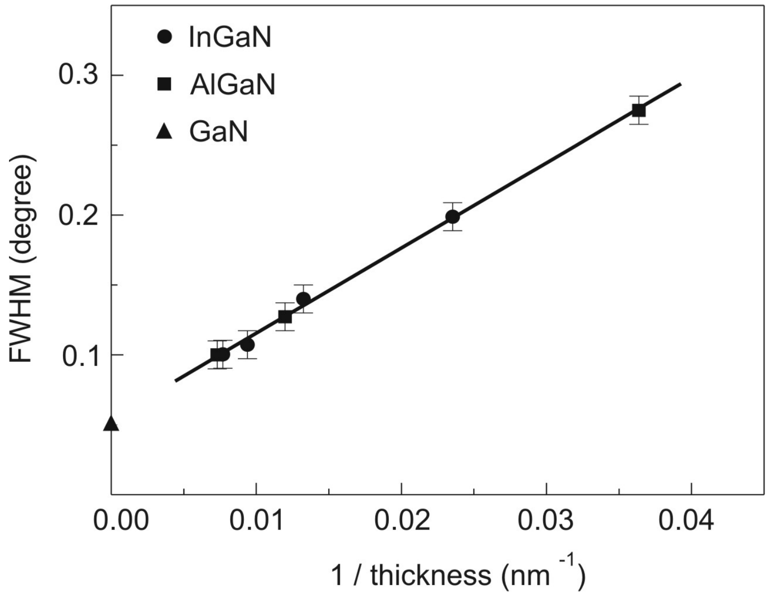

Figure 5.14: Dependence of full width at half maximum of the InGaN and AlGaN peaks from inverse layer thicknesses.

ii) the broadening of the diffraction peaks and the decrease of the scattered X-ray intensity from thin layers limit the minimal layer thickness which can be detected by the IXRD. The X-ray spectra from samples #8 and #9 shown in figure 5.13 indicate that 30 nm thick layers seem to be the detection limit of our IXRD. This means that the IXRD is able to perform online monitoring starting from 30 nm thick InGaN or AlGaN layers. The detection limit can be extended to thinner layers by improving the quality of the Johansson monochromator and increasing the power of the X-ray tube.

As we have shown above, the IXRD offers the potential to obtain information about chemical composition and relative thickness of layers under conditions present in a MOCVD reactor. The chemical composition of epilayers is one of the most important value, because it defines its optical and electrical properties. It is important to be able to identify changes in the chemical composition of the layers during growth in order to influence and correct the growth conditions directly in the growth process. Therefore we have also investigated minimal differences in the composition of layers which can be detected by the IXRD. The resolution in composition determination of the IXRD is limited by the angular resolution of the X'Celerator. The angular resolution of the X'Celerator depends on the distance between pixels of the detector and on the distance between the sample and the detector. The angular resolution of the X'Celerator is 0.01 degree and it corresponds to the resolution in composition determination of AlGaN and InGaN alloys of 0.003 for a chosen reflection. We have measured different InGaN and AlGaN layers which slightly differ in chemical composition. Figure 5.15 shows the results of measurements of samples #10 and #11 which are InGaN layers with a difference in In content of a half percent. We have checked the chemical composition of InGaN alloys by dynamical simulations of high resolution (0002) $\omega - 2\Theta$ scans shown at the right hand side of figure 5.15. The shifting of the InGaN peak due to the change in In content is clearly resolved by the IXRD. Thus these measurement results show that the IXRD has the resolution in chemical composition even better than half percent.

We have performed the same analysis of the resolution limits for AlGaN layers. The X-ray pattern of AlGaN/GaN samples #12 and #13 with a difference in Al content of a half percent are illustrated in figure 5.16. The difference in the position of the AlGaN diffraction peaks is the limit of capabilities of the IXRD, thus half percent is the resolution for the determination of chemical composition of AlGaN alloys.

The difference in resolution of the IXRD setup for InGaN and AlGaN layers is due to the bigger lattice mismatch between InN and GaN lattices than between AlN and GaN.

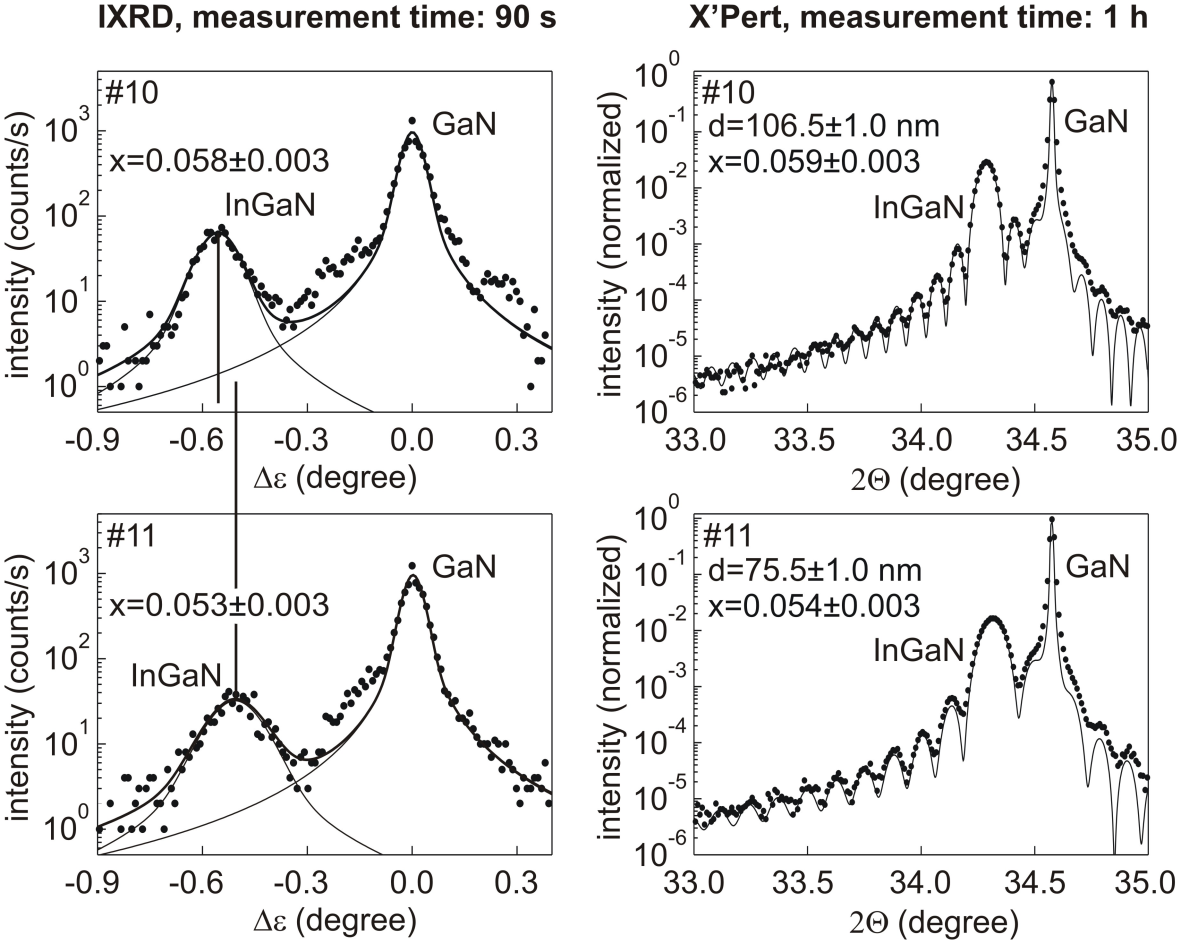

Figure 5.15: The resolution of the IXRD for the control of the chemical composition of the InGaN layers is analyzed. Two InGaN layers which differ in only half percent of In content can be distinguished by the IXRD. The results of IXRD measurements are consistent with the high resolution (0002) $\omega - 2\Theta$ measurements illustrated on the right hand side of the picture.

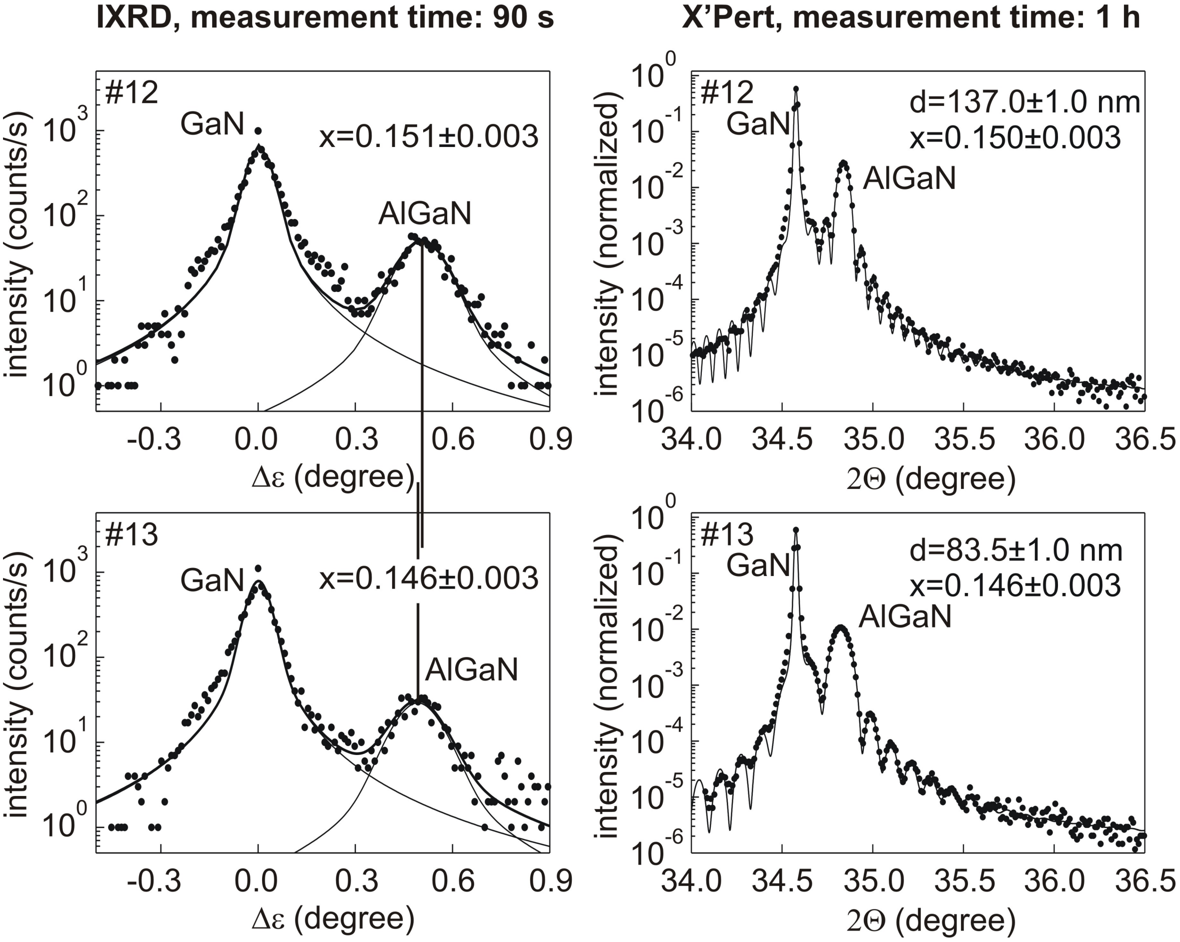

Figure 5.16: The X-ray patterns measured by the IXRD setup (at the left hand side) and by the X'Pert MRD diffractometer (at the right hand side). The difference in the Al content of half percent is still resolved by the IXRD setup and is the limit of IXRD resolution for the control of the chemical composition of AlGaN alloys.

6 Conclusions

A new X-ray diffractometer which allows to perform *in situ* control of the MOCVD growth process using Bragg diffraction of monochromatic X-rays has been realized in this thesis. The principles of work of the new diffractometer and the description of the experimental setup are given in detail. We have developed a model for the interpretation of X-ray spectra taken on the IXRD and have analyzed the possible configuration of the IXRD for controlling the vertical and in-plane features of layered semiconductor structures. We show that the IXRD has a good performance for the diagnostics of epitaxially grown multilayer structures which are used in modern semiconductor industry.

The diffractometer has been tested under conditions typically present in a MOCVD reactor - with rotation and wobble of the samples during measurements. A procedure of X-ray measurements of rotating and wobbling samples has been developed. We have tested our IXRD on different wurtzite type AlGaN and InGaN layers. These materials were chosen because of their successful use for the fabrication of optoelectronic devices. Furthermore, today most of these devices are produced by the MOCVD technology. The tested epilayers were different in composition and thickness allowing to test the IXRD in different aspects. The results show that the IXRD is able to perform the monitoring of the layers with a thickness exceeding 30 nm. The IXRD provides composition and growth rate of the growing layers. We have demonstrated that the IXRD has the same accuracy and the same resolution for composition monitoring as standard high resolution X-ray diffractometers which, however, need much longer measurement times and accurate adjustment of the samples. In the future, the thickness detection limit of 30 nm can be even extended to thinner layers by improving the quality of the Johansson monochromator and increasing the power of the X-ray tube.

Additionally, the particularities of the IXRD allow to use it for fast post-growth characterization of semiconductor materials. We have tested this potential of the IXRD with materials which are important for semiconductor industry today and are grown on a high volume scale. These are InGaN/GaN multiple quantum wells, AlGaN/GaN single heterostructures and SiGe/Si samples. The structural information obtained from the line scans and from reciprocal space maps is in excellent agreement with that gathered from high resolution X-ray diffraction measurements. The IXRD offers advantages which are decisive for the use of the apparatus for fast post-growth diagnostics: very short data collection time, insensitivity to alignment of the samples before measurement and absence of any positioning of the samples during measurement.

We have shown that X-ray diffraction measurements taken on the IXRD provide important structural information even under conditions in a MOCVD reactor. Since this information is not obtainable by other methods, IXRD paves the way for an extensive *in situ* diagnostics of epitaxial processes.

A Lattice parameters and stiffness coefficients of relevant materials

The tables A.1 and A.2 contain lattice and elastic constants of materials relevant for this thesis. For wurtzite type related materials we have used the data reported by O. Ambacher in his review article on group III - nitrides [30]. For SiGe we have applied the data published in [31].

Table A.1: Lattice a_0, c_0 and stiffness C_{11}, C_{13} constants for hexagonal GaN, InN and AlN.

	a_0 (Å)	c_0 (Å)	$C_{11}(GPa)$	$C_{13}(GPa)$
GaN	3.189	5.185	374	70
InN	3.54	5.705	190	121
AlN	3.112	4.982	345	120

Table A.2: Lattice a_0, c_0 and stiffness C_{11}, C_{12} constants for cubic Si and Ge.

	a_0 (Å)	$C_{11}(GPa)$	$C_{12}(GPa)$
Si	5.431	165.8	63.9
Ge	5.6575	128.5	48.3

B Examples of the evaluation of the IXRD spectra

In this part of the appendix we describe the procedure of data interpretation of the measurements performed with the IXRD diffractometer. As examples we consider the IXRD measurements of the AlGaN/GaN single heterostructure as well as of the SiGe/Si sample and give the detailed explanation of how we get the structural information from the spectra measured on the IXRD.

In figure B.1 we depict the $(11\bar{2}4)$ diffraction spectrum of AlGaN/GaN single heterostructure #1 collected on the IXRD. The angular separation between the diffraction peaks of AlGaN and GaN is 0.35 ± 0.01 degree. The accuracy in determination of the angular distance is limited by the resolution of the X'Celerator detector. The distance between the pixels of the detector and the distance between sample and detector correspond to the angular distance between measurement points of 0.01 degree and we consider this angle as a systematic error in determination of the angular position. Following equation 3.3 we calculate the distance $\Delta Q_{IXRD} = 0.0249 \pm 0.0007$ Å^{-1} between reflexes of AlGaN and GaN in reciprocal space. This distance equals the vertical distance ΔQ_z between AlGaN and GaN reflexes multiplied by the geometrical factor of 0.99 for the $(11\bar{2}4)$ reflection as shown in section 3.2. Therefore the vertical position of the AlGaN reflex in reciprocal space is given by $Qz_L = Qz_S + (0.99 \cdot \Delta Q_{IXRD})$ where Qz_S is the vertical position of the GaN reflex which can be calculated for the $(11\bar{2}4)$ reflection by $Qz_S = (8 * \pi)/c_S = (8 * \pi)/5.185 = 4.8472$ Å^{-1}. The vertical position of the AlGaN reflex is $Qz_L = 4.8719$ Å^{-1} and gives access to the vertical lattice parameter of AlGaN layer $c_L = (8 * \pi)/Qz_L = (8 * \pi)/4.8719 = 5.1588 \pm 0.0008$ Å. Thus assuming that the AlGaN layer is fully strained on GaN we have in-plane $a_L = 3.189$ Å and lattice parameter $c_L = 5.1588 \pm 0.0008$ Å perpendicular to the sample surface. Following the formula 2.10 we find the chemical composition of the layer $x = 0.105 \pm 0.003$.

The next example is the evaluation of the (224) diffraction spectrum of SiGe/Si sample #5 shown in figure B.2 which includes the determination of the composition and the

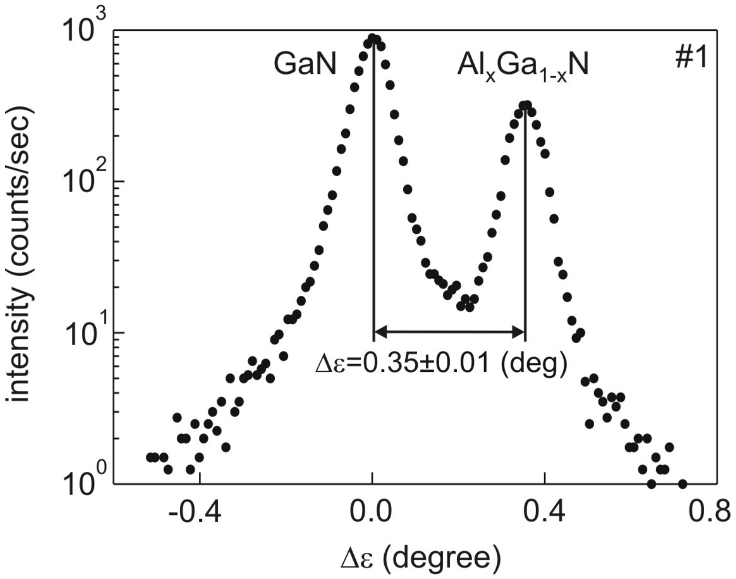

Figure B.1: The diffraction spectrum of an AlGaN/GaN single heterostructure taken on the IXRD. The angular distance between AlGaN and GaN peaks provides the composition of the layer according to the procedure described in the text.

thickness of the SiGe layer. The angular distance between SiGe and Si peaks is 0.76±0.01 degree. Referring to equation 3.3 we find the distance $\Delta Q_{IXRD} = 0.0541 \pm 0.0007$ Å^{-1} between reflexes of SiGe alloy and Si in reciprocal space. From our considerations in section 3.2 and from table 3.2 we know that for the (224) reflection the vertical distance ΔQ_z between the SiGe alloy and the Si reflexes equals ΔQ_{IXRD} distance multiplied by the geometrical factor of 1.02. Knowing the vertical position of the Si reflex in reciprocal space $Qz_S = 4.62765$ Å^{-1} we find the vertical position of the reciprocal lattice point of alloy according to $Qz_L = Qz_S - (1.02 \cdot \Delta Q_{IXRD}) = 4.5725 \pm 0.0007$ Å^{-1}. The vertical lattice parameter c_L of the SiGe layer is directly connected to the vertical position Qz_L and equals $c_L = (8 * \pi)/Qz_L = (8 * \pi)/4.5726 = 5.4965 \pm 0.0008$ Å. Assuming that the layer is fully strained ($a_L = a_S = 5.431$ Å) we have both the vertical $c_L = 5.4965 \pm 0.0008$ Å and the in-plane $a_L = 5.431$ Å lattice parameters of the alloy. According to the formula 2.10 we find the chemical composition of the layer to be $x = 0.163 \pm 0.003$. The angular distance between two subsequent thickness oscillations is 0.17 ± 0.01 degree. This corresponds to the distance in reciprocal space $\Delta Q_{IXRD} = 0.0121 \pm 0.0007$ Å^{-1} and to the vertical distance $\Delta Q_z = 1.02 \cdot \Delta Q_{IXRD} = 0.0123 \pm 0.0007$ Å^{-1} . The vertical distance between thickness oscillations in reciprocal space gives the thickness of the layer by $D = (2 * \pi)/\Delta Q_z = (2 * \pi)/0.0123 = 51 \pm 3\ nm$.

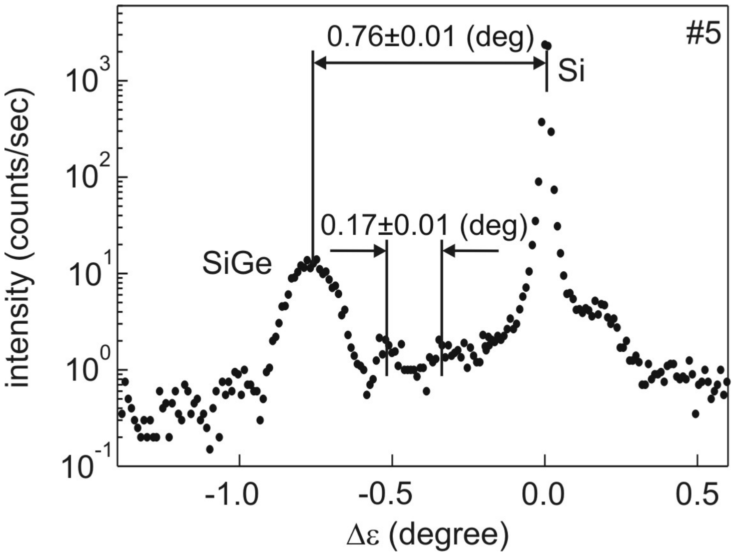

Figure B.2: Measurement result of a SiGe/Si sample. The angular distances between Si, SiGe peaks as well as between two subsequent thickness oscillations give access to the composition and thickness of the alloy.

We follow the same procedure of data interpretation for the measurements of InGaN/GaN multiple quantum wells described in this thesis.

Bibliography

[1] G. Bauer and W. Richter, *Optical Characterization of Epitaxial Semiconductor Layers* (Springer-Verlag, Berlin Heidelberg New York, 1996).

[2] V. Holy, U. Pietsch, and T. Baumbach, *High resolution X-ray scattering from thin films and multilayers* (Springer-Verlag, Berlin, 1999).

[3] D. W. Kisker, P. H. Fuoss, S. Brennan, G. Renaud, K. L. Tokuda, and J. L. Kahn, J. Crystal Growth **101**, 42 (1990).

[4] P. H. Fuoss, D. W. Kisker, G. Renaud, K. L. Tokuda, S. Brennan, and J. L. Kahn, Phys. Rev. Lett. **63**, 2389 (1989).

[5] P. H. Fuoss, D. W. Kisker, F. J. Lamelas, G. B. Stephenson, P. Imperatori, and S. Brennan, Phys. Rev. Lett. **69**, 2791 (1992).

[6] R. L. Headrick, S. Kycia, Y. K. Park, A. R. Woll, and J. D. Brock, Phys. Rev. B **54**, 14 686 (1996).

[7] R. L. Headrick, S. Kycia, A. R. Woll, J. D. Brock, and M. V. Ramana Murty, Phys. Rev. B **58**, 4818 (1998).

[8] G. B. Stephenson, J. A. Eastman, C. Thompson, O. Auciello, L. J. Thompson, A. Munkholm, P. Fini, S. P. DenBaars, and J. S. Speck, Appl. Phys. Lett. **74**, 3326 (1999).

[9] M. V. Ramana Murty, S. K. Streiffer, G. B. Stephenson, J. A. Eastman, G. R. Bai, A. Munkholm, O. Auciello, and Carol Thompson, Appl. Phys. Lett. **80**, 1809 (2002).

[10] A. Munkholm, Carol Thompson, M. V. Ramana Murty, J. A. Eastman, O. Auciello, G. B. Stephenson, P. Fini, S. P. DenBaars, and J. S. Speck, Appl. Phys. Lett. **77**, 1626 (2000).

[11] P. Fini, A. Munkholm, Carol Thompson, G. B. Stephenson, J. A. Eastman, M. V. Ramana Murty, L. Zhao, S. P. DenBaars, and J. S. Speck, Appl. Phys. Lett. **76**, 3893 (2000).

[12] W. L. Bragg, Proc. Cambridge Phil. Soc. **17**, 43 (1913).

[13] B. E. Warren, *X-ray diffraction* (Dover Publications, Inc., New York, 1990).

[14] M. A. Krivoglaz, *X-ray and neutron diffraction in nonideal crystals* (Springer-Verlag, Berlin, 1980).

[15] C. G. Darwin, Phil. Mag. **27**, 675 (1914).

[16] P. P. Ewald, Ann. Physik **54**, 519 (1916).

[17] M. von Laue, Ergeb. d. exakt. Naturw. **10**, 133 (1931).

[18] Z. G. Pinsker, *Dynamical Scattering of X-rays in Crystals* (Springer Verlag, Berlin Heidelberg New York, 1978).

[19] S. Takagi, Acta Cryst. **15**, 1311 (1962).

[20] S. Takagi, J. Phys. Soc. Japan **26**, 1239 (1969).

[21] D. Taupin, Bull. Soc. Fr. Mineral. Crystallogr. **87**, 469 (1964).

[22] V. I. Punegov and A. V. Kharchenko, Crystallography Reports **43**, 1020 (1998).

[23] J. F. Nye, *Physical Properties of Crystals, Their representation by tensors and matrices* (Oxford University Press, London, 1957).

[24] A. Pesek, Ph.D. thesis, Johannes Kepler University, Linz, Austria, 1993.

[25] M. Schuster, P. O. Gervais, B. Jobst, W. Hsler, R. Averbeck, H. Riechert, A. Iberl, and R. Stmmer, J. Phys. D: Appl. Phys. **32**, A56 (1999).

[26] T. Johansson, Z. Phys. **82**, 507 (1933).

[27] S. Nakamura, M. Senoh, S. Nagahama, N. Iwasa, T. Yamada, T. Matsushita, Y. Sugimoto, and H. Kiyoku, Appl. Phys. Lett. **69**, 4056 (1996).

[28] M. Kneissl, D. Bour, C. Van de Walle, L. Romano, J. Northrup, R. Wood, M. Teepe, and M. Johnson, Appl. Phys. Lett. **75**, 581 (1999).

[29] U. Niggemeier, Ph.D. thesis, University of Paderborn, Paderborn, Germany, 1999.

[30] O. Ambacher, J. Phys. D: Appl. Phys. **31**, 2653 (1998).

[31] *Properties of strained and relaxed Silicon Germanium*, edited by E. Kasper (INSPEC, the Institution of Electrical Engineers, London, United Kingdom, 1995).

List of Publications

A. Pawlis, A. Khartchenko, O. Husberg, D. J. As, K. Lischka, D. Schikora, "Large room temperature Rabi-splitting in a ZnSe/(Zn, Cd)Se semiconductor microcavity structure". Solid State Communications 123, 235 (2002)

A. Tabata, L. K. Teles, L. M. R. Scolfaro, J. R. Leite, A. Khartchenko, T. Frey, D. J. As, D. Schikora, K. Lischka, J. Furthmüller, and F. Bechstedt, "Phase separation suppression in InGaN epitaxial layers due to biaxial strain". Appl. Phys. Lett. 80, 769 (2002)

O. Husberg, A. Khartchenko, H. Vogelsang, D. J. As, K. Lischka, O. C. Noriega, A. Tabata, L. M. R. Scolfaro, J. R. Leite, "Photoluminescence associated with quantum dots in cubic GaN/InGaN/GaN double heterostructures". Physica E 13, 1090 (2002)

O. C. Noriega, J. R. Leite, E. A. Meneses, J. A. N. T. Soares, S. C. P. Rodrigues, L. M. R. Scolfaro, G. M. Sipahi, U. Köhler, D. J. As, S. Potthast, A. Khartchenko, and K. Lischka, "Photoluminescence and Photoreflectance Characterization of Cubic $GaN/Al_xGa_{1-x}N$ Quantum Wells". phys. stat. sol. (c) 0, 528 (2002)

O. Husberg, A. Khartchenko, D. J. As, K. Lischka, E. Silvera, O. C. Noriega, J. R. L. Fernandez, and J. R. Leite, "Thermal Annealing of Cubic InGaN/GaN Double Heterostructures". phys. stat. sol. (c) 0, 293 (2002)

D. J. As, U. Köhler, S. Potthast, A. Khartchenko, K. Lischka, V. Potin, and D. Gerthsen, "Cathodoluminescence, High-Resolution X-ray Diffraction and Transmission-Electron-Microscopy Investigations of Cubic AlGaN/GaN Quantum Wells". phys. stat. sol. (c) 0, 253 (2002)

U. Köhler, D. J. As, S. Potthast, A. Khartchenko, K. Lischka, O. C. Noriega, E. A. Meneses, A. Tabata, S. C. P. Podrigues, L. M. R. Scolfaro, G. M. Sipahi, and J. R. Leite, "Optical characterization of cubic AlGaN/GaN Quantum Wells". phys. stat. sol. (a) 192, 129 (2002)

O. Husberg, A. Khartchenko, D. J. As, H. Vogelsang, T. Frey, D. Schikora, and K. Lischka, O. C. Noriega, A. Tabata, and J. R. Leite,
"Photoluminescence from quantum dots in cubic GaN/InGaN/GaN double heterostructures". Appl. Phys. Lett. 79, 1243 (2001)

A. Pawlis, O. Husberg, A. Khartchenko, K. Lischka, and D. Schikora,
"Structural and Optical Investigations of ZnSe Based Semiconductor Microcavities". phys. stat. sol. (a) 188, 983 (2001)

A. Kharchenko, U. Englisch, Th. Geue, J. Grenzer, U. Pietsch, R. Siebrecht,
"Investigation of Partially Deuterated Organic Multilayers by Means of X-ray and Polarized Neutron Reflectometry". Neutron News 11, 29 (2000)

V. I. Punegov, A.V. Kharchenko,
"Effect of Multiple Diffuse Scattering on the Dynamical Diffraction of X-rays in Non uniform Layer Crystals Containing Microdefects". Crystallography Reports 43, 1020 (1998)

Acknowledgements

First and foremost, I would like to thank sincerely Prof. Dr. Klaus Lischka for the possibility to work in his group, for valuable advises and discussions during my work on this PhD thesis.

I thank appl. Prof. Dr. Donat As for helpful discussions.

Special thanks go to S. Igges for his suggestions during the construction of X-ray diffractometer.

J. Bethke , J. Woitok (PANalytical B.V., The Netherlands) for a good cooperation during European Project.

K. Schmidegg and Prof. H. Sitter (University of Linz, Austria) for a good cooperation during the work at University of Linz.

I also want to thank B. Volmer, I. Zimmermann for their help in solving bureaucratical and technical problems.

I would like to express my gratitude to the PhD students O. Husberg, A. Pawlis, S. Potthast, Shunfeng Li and to the master degree student J. Schörmann for their helpful discussions.